water

MDPI

Article

Flood-Induced Scour Failure Mechanisms and Multi-Level Protection of Riverside Highway Embankments: A Physical Model Study

Peifeng Han [1], Wenrui Gao [1], Song Gu [1,*], Haitao Xu [2], Shasha Yi [2] and Songbo Ren [1]

[1] School of Civil Engineering and Architecture, Southwest University of Science and Technology, Mianyang 621010, China
[2] Mianyang Chuanjiao Highway Planning, Survey and Design Co., Ltd., Mianyang 621000, China
* Correspondence: gusong@swust.edu.cn

Abstract

Scaled flume tests based on Froude similarity (λ = 1:50) were conducted to clarify the internal stress-field evolution and multi-level protection mechanisms during flood scour of riverside highway embankments. An 18-channel miniature earth-pressure system embedded along the slope, with dual-view cameras, provided synchronous acquisition. Six non-replicated tests covered three protection levels (unprotected; semi-protected with gabion and geotextile; fully protected with an additional spur dike) at three flow velocities, yielding approximately 288,000 time-series readings (about 16,000 synchronous time steps). Scour failure followed a unified four-stage evolution: flow establishment and seepage onset, scour expansion and toe instability, progressive collapse and failure surface extension, and scour-hole stabilization with residual transport. Increasing velocity accelerated failure and shifted the mode from progressive toe scour to rapid retrogressive erosion. Protection structures exerted a dual effect, delaying failure at low velocities through weight stabilization and energy dissipation but potentially intensifying local scour at high velocities through flow concentration. Using internal earth pressure and higher-order statistical moments, a preliminary criterion distinguishing surface scour from internal erosion was proposed. The weight-stabilizing effect of the gabion self-weight was quantitatively characterized. AI1-13 was identified as a candidate early-warning sensor, and a dual warning signal (rise-then-fall and skewness reversal) was observed. A tentative three-level early-warning framework is proposed. Owing to the non-replicated, reduced-scale nature of the tests, these quantitative indicators are presented as preliminary bounds rather than validated field thresholds. The findings clarify embankment protection failure mechanisms and highlight the influence of hydraulic intensity and protection configuration on scour resistance.

Keywords: riverside embankment; flood scour; gabion protection; skewness analysis; early-warning criterion

Check for updates

Academic Editor: Jueyi Sui

Received: 8 September 2026
Revised: 1 October 2026
Accepted: 10 October 2026
Published: 12 October 2026

Copyright: © 2026 by the authors. Licensee MDPI, Basel, Switzerland. This article is an open access article distributed under the terms and conditions of the Creative Commons Attribution (CC BY) license.

1. Introduction

Flooding is among the most severe and recurrent natural hazards and poses a major threat to transportation infrastructure worldwide. Highway systems are particularly vulnerable to floods because of their linear alignment, limited structural redundancy, and heavy dependence on continuous subgrades and drainage systems. Typical examples are the Beichuan section of National Highway G347 and the Pingwu section of Provincial Highway S205 in western Sichuan, China, which lie in the transition zone between the

Longmenshan fault belt and the Sichuan Basin, where deeply incised V-shaped valleys result in riverside subgrades accounting for more than 40% of the route length; these sections experienced repeated flood-induced road closures in 2019, 2021, and 2023. Globally, the increasing frequency of extreme rainfall events is exacerbating such risks [1], with flood-related damage accounting for more than 60% of bridge and road failure events [2,3]. These events highlight the persistent vulnerability of highway subgrades under extreme hydrological loading and the urgent need to understand the scour failure mechanisms of riverside subgrades during floods.

Riverside subgrades are highly prone to progressive flood-induced damage. Scour failure generally follows a progressive sequence of toe undercutting, slope instability, and progressive collapse, which is mechanistically consistent with the theoretical framework of bank stability and progressive failure proposed by Rinaldi and Darby [4] and the scour–pore-pressure positive-feedback mechanism of Simon et al. [5]. Through 1:2-scaled flume tests on overtopped ballast railway embankments, Suchada Wutti confirmed that breach development under overtopping flows exhibits a distinct four-stage sequence: initial flow development and seepage emergence, overtopping-induced collapse, secondary failure and breach widening, and flow stabilization and residual transport, indicating the combined effects of hydraulic discharge and sleeper configuration on the breach evolution of ballast-filled railway embankments [6]. Regarding scour mechanisms, Briaud et al., based on the classical framework of incipient particle motion, established the quantitative Vc–D_{50} relationship through erosion function apparatus (EFA) tests and classified scour failure into surface erosion and internal erosion, including piping and soil boiling [7–9].

Extensive research has been devoted to assessing flood-induced scour of embankment slopes. Mohammadnezhad et al. [10] further confirmed that riprap thickness and tailwater depth are the two most sensitive parameters governing riprap protection performance, and that increasing riprap thickness can reduce scour depth by nearly 90%. For abutment scour, Ettema et al. [11,12] and Idil-Bektur [13] revealed the excessive fragility bias of abutment embankments and the fundamental limitation of riprap protection. Even where the armor layer remains structurally sound, interfacial discontinuities between the armor and subsoil may induce global embankment failure. Regarding protection measures, Freeman and Fischenich [14] systematically evaluated the applicability of gabions for bank scour protection and highlighted their flexibility and permeability advantages in energy dissipation; Lagasse [15] and Melville et al. [16] studied the critical stability of armor materials from the perspective of riprap size selection and design specifications. Kuhnle et al. [17] and Duan [18] revealed the hydraulic characteristics of flow around spur dikes and the velocity decay in the downstream recirculation zone. Gao et al. [19] systematically verified the individual effects of the above protection elements and the key role of geotextile wrapping through 14 flume tests. Sherzai et al. [20] further demonstrated that placing geogrids or rigid aprons downstream of an embankment can reduce the maximum scour depth by up to 100%, but this strategy is a downstream passive protection fundamentally different from the combined protection strategy in this study, which integrates active energy dissipation on the slope, basal isolation, and flow-direction regulation. At the field scale, recent studies on the cascading flood impacts of potential landslide dams [21] and on rainfall-induced regional slope instability [22] highlight that natural failure scenarios are governed by unsteady discharge and spatially heterogeneous boundary conditions, which differ fundamentally from the constant-velocity, homogeneous conditions adopted in the present controlled flume study.

Although the above studies demonstrate that floods induce a series of scour-related degradation phenomena in embankments, existing research still has five shortcomings. First, real-time synchronous monitoring of the internal earth pressure within the slope is

completely absent; both scour mechanism studies [10] and protection verification studies [19,20] rely solely on point velocity measurements, water level records, and visual imaging, which cannot provide direct information on whether the soil stress beneath the scour hole has reached the critical instability threshold. Second, whether multiple protection elements act synergistically or counteract each other lacks systematic orthogonal experimental separation. Third, the mechanical mechanisms underlying the effectiveness of protection structures remain at a qualitative level; how the self-weight preload of a gabion establishes a compressive stress field in the soil and how the velocity reduction behind a spur dike can be quantified as stress unloading both lack direct experimental evidence. Fourth, there is a quantitative gap between laboratory-based stability/failure judgments and the decision of when to initiate traffic control in the field; hydraulic-parameter warnings based on water level or velocity are indirect, whereas structural-mechanical warnings based on earth pressure signals can directly indicate the disappearance of the load-bearing medium. Fifth, how the excessive fragility bias of scaled embankments identified by Ettema [11] propagates and affects conclusions under multiple working conditions and protection levels also lacks quantitative evaluation.

To address these shortcomings, this study systematically evaluates and characterizes the scour failure mechanisms and the protective performance of multi-level protection systems for riverside highway subgrades through scaled physical model tests in a laboratory open-channel flume. Continuous constant-velocity scour conditions were adopted to simulate progressive flood loading, and three protection configurations were tested: unprotected, semi-protected (gabion + geotextile), and fully protected (a spur dike added to the semi-protected configuration). By applying three flow velocities of 0.2, 0.4, and 0.8 m/s, the influence of hydraulic intensity and protection level on the initiation and expansion of failure was investigated. For the first time, an 18-channel multi-source synchronous earth pressure acquisition system embedded along the slope was integrated inside a scaled embankment model, focusing on key failure behaviors including failure mechanisms, the spatiotemporal evolution of the internal stress and seepage fields, higher-order statistical characteristics such as skewness, failure propagation laws, and the mechanical action of the protection structures.

2. Materials and Methods

2.1. Experimental Design

2.1.1. Physical Model

The prototype of this test is a riverside highway embankment slope protection project in the mountainous region of western Sichuan, designed in accordance with relevant river regulation specifications, with a slope gradient of 1:1.7 (vertical:horizontal). The indoor physical model was designed based on the Froude similarity criterion [23] with a uniform geometric scale of λ = 1:50, corresponding to a velocity scale of $\lambda v = \lambda \hat{} 0.5 \approx 1{:}7.07$. The key model dimensions are: slope height 300 mm, base thickness 100 mm, riverbed sand width 290 mm, retaining wall width 200 mm, and total model width 1000 mm, fully preserving the 1:1.7 prototype slope gradient and overall geometric characteristics to ensure geometric similarity; the model cross-section is shown in Figure 1.

Three protection conditions were designed: Model a is an unprotected bare slope (corresponding to condition G1 below), Model b is a semi-protected slope with a toe gabion (corresponding to G2 and G3), and Model c is a fully protected slope with a gabion and a spur dike (corresponding to G4, G5, and G6). Under this scaling, the model Reynolds number is about 1/353 of the prototype; however, the Reynolds numbers of all test conditions exceed 104, satisfying the fully developed turbulent flow condition, so the influence of viscous forces is negligible [24] and the Froude similarity criterion is applicable. Because

the scaled model soil lacks prototype cohesion and its structural strength is relatively weak [11] the critical scour velocity obtained in this test is conservative when extrapolated to the prototype. This similarity treatment is consistent with the conclusions of existing turbulent scour model tests [19]; however, as detailed in Section 2.3, Froude similarity cannot simultaneously scale sediment mobility, pore-pressure response, seepage time scale, and soil strength, so the model reproduces the dominant gravity-driven flow-scour and failure patterns qualitatively, while quantitative extrapolation to the prototype requires the scaling corrections discussed below.

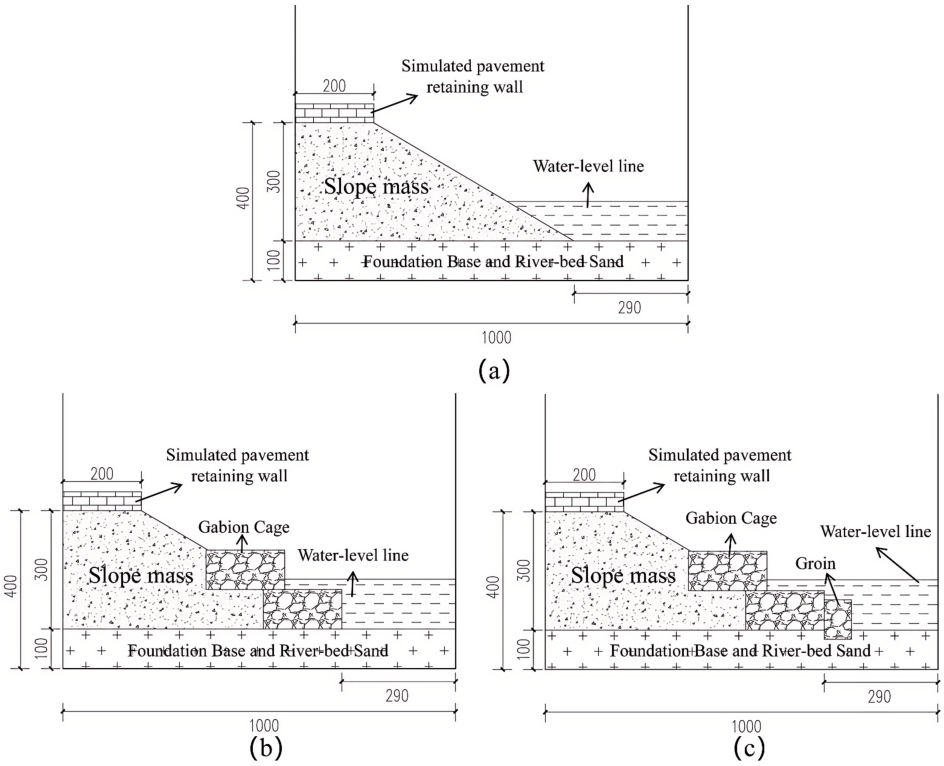


Figure 1. Cross-section of the 1:50 physical model: (**a**) unprotected bare slope; (**b**) semiprotected slope with a toe gabion; (**c**) fully protected slope with a gabion and a spur dike (unit: mm).

For data processing, the generative-AI assistant DeepSeek was used to assist in organizing and screening the sensor time-series data (data sorting, deduplication, and preliminary outlier identification). The authors subsequently reviewed and verified all data and analyses, and take full responsibility for the accuracy and integrity of the results.

2.1.2. Protection Scheme Design

The three progressively increasing protection levels constitute a complete three-tier protection spectrum from none to full protection. The unprotected case (G1) is a bare slope control. The semi-protected case (G2, G3) includes a gabion revetment (model size 1500 × 200 × 100 mm, stainless steel wire mesh with 2 mm openings (Jinbin Wire Mesh Products Co., Ltd., Anping, China), filled with 3–5 mm gravel at a porosity of 30–40%, arranged in two rows and two columns) and a nonwoven geotextile (200 g/m^2, Dingji New Material Technology Co., Ltd., Changzhou, China) on the slope surface. The steel wire mesh integrates the loose gravel into a structurally integral flexible panel [14], systematically avoiding the common failure mode in which soil particles of a riprap cushion are lost through the gaps between stones [15]. The fully protected case (G4, G5, G6) adds an upstream spur dike to the semi-protected configuration (dike length approximately 1/4 to 1/3 of the gabion width), which uses the hydraulic principle of flow diversion to deflect the

high-velocity main flow away from the slope toe and form a hydrodynamic shadow zone at the toe [17,18]. The installation state of the three protection systems is shown in Figure 2.



(**a**) (**b**) (**c**)

Figure 2. Installation state of the three protection configurations: (**a**) unprotected; (**b**) semi-protected (gabion + geotextile); (**c**) fully protected (gabion + spur dike).

2.1.3. Material Properties

The fill soil used in this study was collected from the Beichuan section of National Highway G347 in western Sichuan. Coarse particles larger than 5 mm were removed and the fine fraction was retained, with D_{50} of 1.2 mm and a uniform compaction degree of 90%. The full grain-size distribution curve (Figure 3), uniformity coefficient (Cu), dry density, void ratio, saturated hydraulic conductivity, water content, effective friction angle (φ′), and effective cohesion (c′) of the fill are summarized in Table 1; these data are required to reproduce the surface-erosion versus internal-erosion distinction [7–9]. According to the Vc–D50 relationship of Briaud et al. [8], the critical velocity of this material on a flat bed is approximately 0.3–0.5 m/s, providing the basis for the selection of subsequent flow velocity conditions. The gabion filling gravel is 3–5 mm in diameter with a porosity of 30–40%; the geotextile is a 200 g/m^2 nonwoven type; and the wire mesh openings are 2 mm.

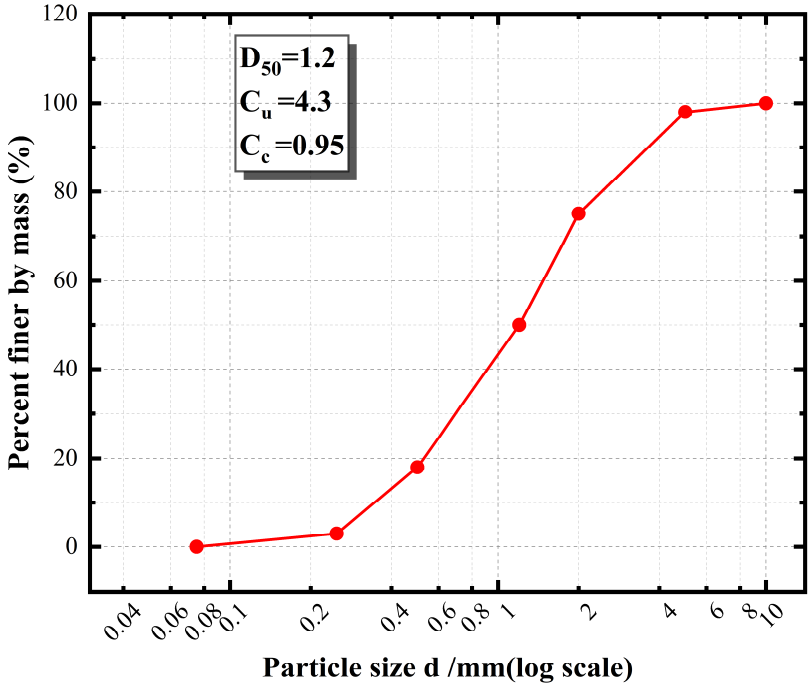


Figure 3. Grain-size distribution of the fill material (SP, poorly graded sand).

Table 1. Geotechnical index properties of the fill material.

Property	Value
Soil classification (USCS)	SP (poorly graded sand)
Median grain size D_{50}	1.2 mm
D_{10}	0.35 mm
D_{30}	0.69 mm
D_{60}	1.47 mm
Uniformity coefficient C_u	4.3
Coefficient of curvature Cc	0.95
Gravel content (>4.75 mm)	3.3%
Fines content (<0.075 mm)	0%
Dry density ρd	1.62 g/cm^3
Void ratio e	0.63
Saturated hydraulic conductivity k	3×10^{-4} m/s
Natural water content w	12%
Effective friction angle φ′	33°
Effective cohesion c′	≈0 kPa (non-cohesive)
Critical Shields parameter θcr	0.03–0.04

Note: the grain-size distribution and USCS classification are based on the sieve analysis of the Beichuan fill material.

2.2. Experimental Setup and Procedure

2.2.1. Test Apparatus and Monitoring System

The test flume (self-manufactured, Southwest University of Science and Technology, Mianyang, China) uses a steel frame with high-transmittance tempered glass side walls, a clear opening of 100 cm × 70 cm, and a test section approximately 15 m long. The water supply system is a closed loop. Flow velocity was measured with a propeller-type current meter (Hydrological Instrument Factory of Nanjing Hydraulic Research Institute, Nanjing, China) at the approach cross-section at 60% of the flow depth, and the cross-sectionally averaged velocity was obtained by velocity-area integration over five verticals. The discharge was set by the pump frequency and verified with an electromagnetic flowmeter (Beijing Far East Instrument Co., Ltd., Beijing, China), and the approach flow was confirmed to be approximately uniform across the width (lateral variation <5%). The upstream and downstream water levels were monitored with point gauges during each test; the flow-velocity calibration deviation was within ±5%. The flume bottom is kept at zero slope to reproduce low-slope scour conditions; the overall configuration is shown in Figure 4.

Eighteen miniature earth pressure sensors (28 mm diameter, ±50 kPa range, ±0.1% FS, Danmo Electronic Technology Co., Ltd., Nanjing, China) were installed. In the recorded signals, negative readings correspond to compressive stress and positive readings to tensile (outward) stress on the sensing membrane; this sign convention follows the raw transducer output and was verified by pre-test calibration Before each test series, all 18 sensors were calibrated in a dead-weight loading frame over the full ±50 kPa range in 10 kPa increments; the calibration curves were linear ($R^2 > 0.999$), with a zero drift below 0.01 kPa over a 1 h stability check and a hysteresis below 0.5% FS. The sensors were waterproofed with a silicone coating, oriented with the sensing membrane normal to the slope surface, and installed in horizontal layers during compaction so that the membrane remained in full contact with the surrounding soil without disturbing the local density. The sensors measure the total normal stress on the membrane; because pore-water pressure was not independently recorded, the readings are total-stress responses that include hydrodynamic and seepage-pressure components and are not decomposed into effective soil-skeleton stress; pore-water pressure was therefore not decoupled from the readings, and the pore-pressure dynamics remain an unmeasured coupled variable longitudinally along the slope

surface in the middle cross-section of the slope (1/2 width, to eliminate side-wall boundary effects). They were numbered AI1-1 to AI1-18. Their roles are summarized in Table 2, and their spatial layout is shown in Figure 4. The sensors were arranged along the slope surface (the slope surface is approximately 59 cm long, with a slope height of 30 cm and a gradient of 1:1.7). AI1-4 serves as the core measurement point, recording the largest response; AI1-9, with a much smaller response, is used together with AI1-4 to distinguish surface erosion from internal scour; AI1-13 reflects the propagation of toe failure into the slope earlier, serving as the early-warning sensor. With dual-view cameras, all channels were synchronously sampled at 2 Hz, yielding approximately 288,000 time-series readings (about 16,000 synchronous time steps across the 18 channels).

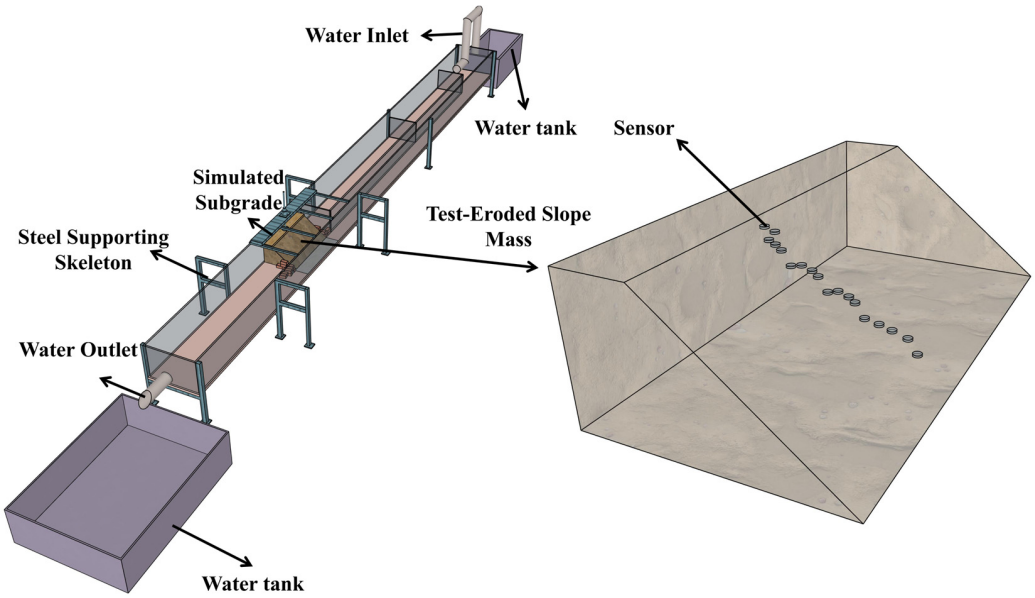


Figure 4. Overall layout of the flume scour test system. Spatial layout of the 18 earth pressure sensors along the slope surface.

Table 2. Roles of the 18 sensors, grouped by response magnitude.

Sensor ID	Role
AI1-1, AI1-2, AI1-3	Reference baseline (negligible response, <0.02 kPa throughout)
AI1-4	Core sensor: internal scour (largest response, ~7.6 kPa on average)
AI1-9	Surface erosion (small response, ~230-fold smaller than AI1-4)
AI1-10, AI1-12, AI1-13, AI1-16	Failure propagation (strong response, 0.4–1.0 kPa; AI1-13 is the early-warning sensor)
AI1-11, AI1-14, AI1-15, AI1-17, AI1-18	Moderate response (0.1–0.3 kPa)
AI1-5, AI1-6, AI1-7, AI1-8	Weak/negligible response (<0.06 kPa)

2.2.2. Test Conditions and Procedure

Six test conditions were designed (Table 3). A stable flow was formed by adjusting the water supply discharge so that the flow produced continuous scour conditions along the slope toe. The design logic includes two progressive dimensions: the protection-level dimension (G1, G2, and G4 are all at 0.2 m/s, used to separate the independent contribution of each protection level) and the velocity dimension (G2/G3 and G4/G5/G6 determine the critical scour resistance range by increasing the velocity). During each test, water was

continuously supplied while earth pressure and video were synchronously acquired. If the slope failed (e.g., toe collapse, piping, or geotextile instability), the test was stopped after failure was completed and the condition was judged as failure; if the slope remained stable, water was continuously supplied and recorded until the stress and deformation tended to stabilize, after which the test was stopped and the condition was judged as stable. The actual duration and final state of each condition are given in Table 3.

Table 3. Test condition matrix.

Condition	Protection Level	Model Velocity (m/s)	Prototype Velocity (m/s)	Simulated Condition	Duration (s)	Result
G1	Unprotected	0.2	1.4	Natural weather	716.5	Failure
G2	Semi-protected (gabion + geotextile)	0.2	1.4	Natural weather	1470.5	Stable
G3	Semi-protected (gabion + geotextile)	0.4	2.8	Rainy	1955.5	Failure
G4	Fully protected (+ spur dike)	0.2	1.4	Natural weather	2125.5	Stable
G5	Fully protected (+ spur dike)	0.4	2.8	Rainy	1067.0	Stable
G6	Fully protected (+ spur dike)	0.8	5.7	Rainstorm flood	626.5	Failure

2.3. Similarity, Scaling Distortions, and Flume Confinement

Froude similarity guarantees dynamic similarity only for flows dominated by gravity and inertia; it cannot simultaneously preserve sediment transport, seepage, and soil-mechanics similitude when the model uses the same water and soil as the prototype at a reduced length scale [24]. With λ = 1:50 and a velocity scale $\lambda v = \lambda \hat{} 0.5 \approx 1{:}7.07$, the model Reynolds number is about 6×10^4, 1.2×10^5, and 2.4×10^5 at 0.2, 0.4, and 0.8 m/s (flow depth 0.25–0.35 m), i.e., about 1/353 of the prototype values (2.1×10^7, 4.2×10^7, and 8.6×10^7 at 1.4, 2.8, and 5.7 m/s); both exceed 10^4, so fully turbulent flow is preserved, but the viscous sublayer and boundary-layer thicknesses are not. The Froude number is matched (0.12–0.47 in both model and prototype). By contrast, the grain Reynolds number $Re^* = u^* D_{50}/\nu$ and the Shields parameter $\theta = \tau_0/[(\rho s - \rho) g D_{50}]$ are not preserved: the model grain size $D_{50} \approx 1.2$ mm was not reduced by λ, so the dimensionless Shields number falls in a different sediment-transport regime than the prototype, and incipient-motion and transport rates are only approximately similar (Table 4). The seepage (Darcy) time scale $t_{seep} \propto L^2/(k\Delta h)$ scales as λ^2 rather than the Froude time scale $\lambda \hat{} 0.5$, so pore-pressure response and seepage-induced piping develop on a distorted time base. Following Zhao et al. [25], spatially heterogeneous seepage and preferential flow paths cannot be captured by a single characteristic length; the piping paths observed here should therefore be regarded as qualitative representations of preferential seepage rather than dynamically scaled reproductions. The fill soil also lacks the prototype cohesion [11], and the commercial geotextile and wire mesh are far stiffer than a Froude-scaled equivalent. Consequently, the tests reproduce the dominant gravity-driven scour geometry and the staged failure sequence, whereas sediment-mobility thresholds, pore-pressure magnitudes, and the quantitative stress levels should be interpreted as qualitative to semi-quantitative.

Table 4. Dimensionless similarity parameters for the model and the assumed prototype.

Parameter	Definition	Model	Prototype	Distortion
Froude number Fr	$V/\sqrt{(gh)}$	0.12–0.47	0.12–0.47	1 (matched)
Reynolds number Re	VL/ν	6×10^4–2.4×10^5	2.1×10^7–8.6×10^7	≈1/353
Shields parameter θ	$\tau_0/[(\rho s - \rho)gD_{50}]$	not directly measured	-	not preserved (D_{50} unscaled)
Grain Reynolds number Re*	u^*D_{50}/ν	not directly measured	-	not preserved (D_{50} unscaled)
Seepage time scale	$\propto L^2/(k\Delta h)$	-	-	λ^2 vs. λ^0.5 (distorted)

Note: θ and Re* require the bed shear velocity u*, which was not directly measured (no ADV/PIV); they are reported as 'not directly measured', and the D_{50} scaling violation implies that these groups are not preserved even qualitatively.

Second, the 1.0 m-wide flume laterally confines the flow. The embankment occupies an erodible bed width of about 290 mm, and the spur dike protrudes a further ~150 mm into the channel; combined with the slope and retaining-wall footprint, the cross-sectional constriction ratio (obstructed area/total cross-sectional area) is about 20% for the unprotected case, 25% for the semi-protected case, and 30–45% for the fully protected case (the spur dike alone adds roughly 15%) at the test section. Open-channel guidance indicates that obstruction ratios exceeding ~10–15% induce substantial lateral contraction, backwater, and accelerated bypass velocities [17,24]. The resulting flow concentration along the exposed side of the embankment amplifies local velocities and bed shear stress near the toe; the measured failure velocities and stress levels are therefore specific to this confined geometry and should not be extrapolated to a wide channel without a blockage correction.

For these reasons, the 'critical velocities' reported below are preliminary bounds for the specific model material and this particular flume, and must not be read as validated prototype thresholds.

3. Results

Among the six conditions, G1, G3, and G6 failed, while G2, G4, and G5 remained stable throughout. All three failure conditions exhibited a unified four-stage mode: initial flow establishment and seepage onset, scour expansion and toe instability, progressive collapse and failure surface extension, and scour-hole stabilization with residual sediment transport. This section successively describes the overall evolution of scour failure, the failure mechanisms of each protection level, seepage effects, mechanical response time-history characteristics, and higher-order statistical characteristics.

3.1. General Framework of Scour Failure and the Special Vulnerability of Riverside Subgrades

Flow-induced failure of non-cohesive slopes is generally described as a series of successive stages: downslope erosion, gully incision and retrogressive erosion, retreat of the erosion path accompanied by crest lowering, and lateral expansion toward a quasi-stable failure morphology. Within this framework, riverside highway subgrades exhibit a unique hydraulic vulnerability because their slope toe is directly exposed to flow action: failure typically starts with toe scour, followed by slope instability and progressive expansion upstream.

It is noteworthy that in this test, the internal stress of G1 did not immediately become unstable after a visible scour hole appeared; there was a clear time-sequence difference between the formation of the scour hole and internal mechanical instability; in the first stage, the earth pressure of AI1-4 fluctuated only slightly within ±1 kPa, whereas structural

instability was not concentrated until the third stage. This finding can only be obtained under internal mechanical monitoring, highlighting the unique value of internal stress monitoring for identifying the failure process of riverside subgrades. The failure modes of the three failure conditions are logically consistent with the failure sequences observed by Gao et al. [19] and Tsubaki [26]. The stress distribution of all conditions is shown in Figure 5.

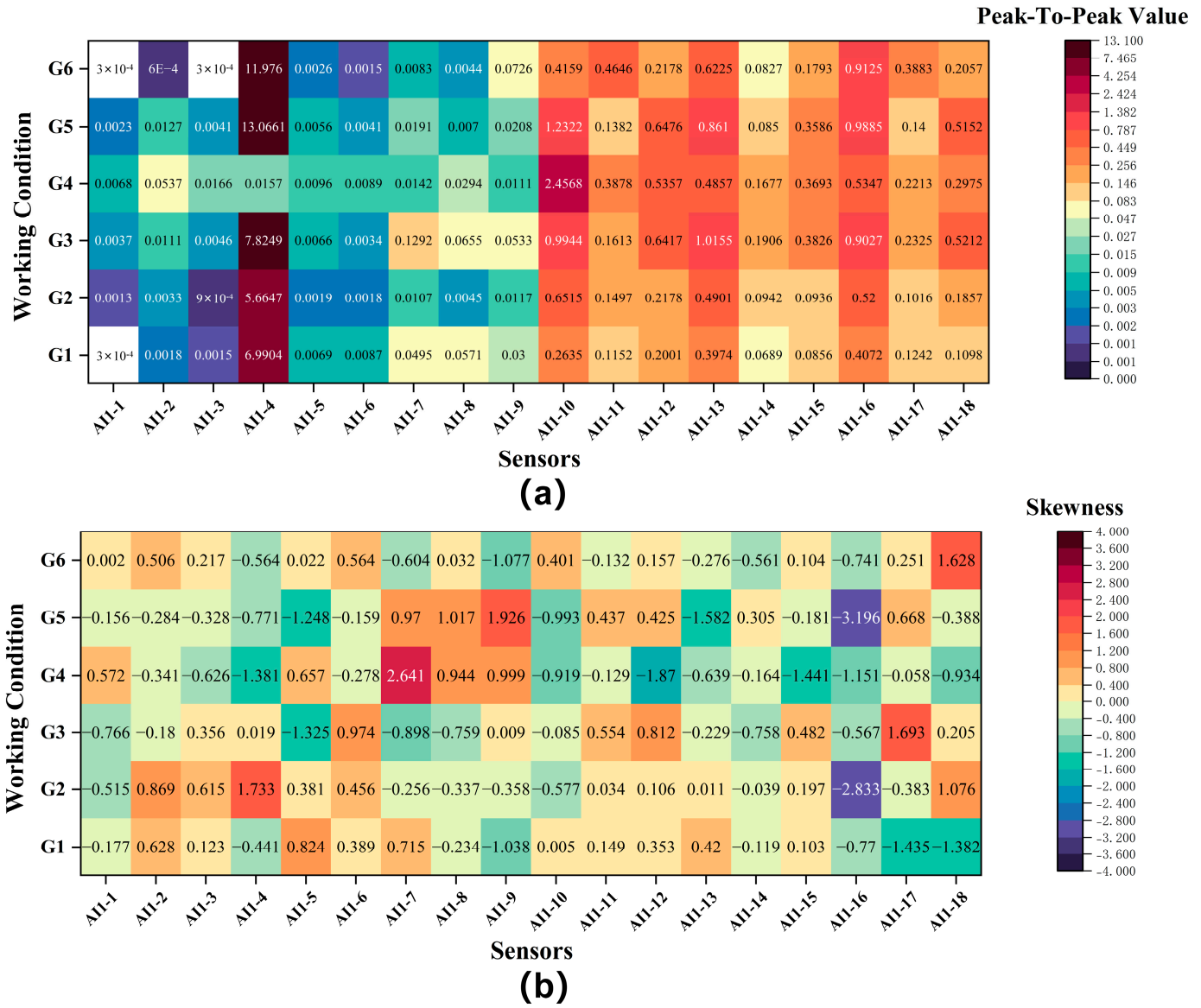


Figure 5. Overview heatmap of the six conditions (18 sensors × 6 conditions): (**a**) peak-to-peak values (log scale); (**b**) skewness (blue = flow-impacted and loose, red = compressed and stable).

Figure 5 presents the overview heatmap of the six conditions. In the peak-to-peak panel (Figure 5a), the response is overwhelmingly concentrated in AI1-4, which dominates the entire map in all six conditions, whereas all other sensors remain below 0.5 kPa, confirming that the mechanical influence of scour is highly localized. The three failure conditions (G1, G3, G6) exhibit strong responses, while the three stable conditions (G2, G4, G5) show suppressed responses through distinct mechanisms: G4 is nearly static (AI1-4 = 0.016 kPa, close to the noise floor) owing to spur dike flow diversion, whereas G5 reaches the highest AI1-4 value (13.07 kPa) despite remaining stable, reflecting the load carried by the protection structure rather than soil scour. In the skewness panel

(Figure 5b), the sign reversal of AI1-4 from G1 (−0.44, flow-impacted and loose) to G2 (+1.73, compressed and stable) is the most prominent feature, quantitatively capturing the weight-stabilizing effect of the gabion; G6 turns negative again, consistent with the re-emergence of failure.

3.2. Failure Mechanisms

3.2.1. Unprotected Subgrade Series (G1, v = 0.2 m/s)

G1 collapsed as a whole after 716.5 s because of excessive toe undercutting, establishing the reference baseline for the entire test. The failure process showed a clear four-stage progressive evolution. Stage 1 (initial flow establishment and seepage onset): the near-bed velocity reached the critical incipient motion condition of sand particles (the θcr range of Briaud et al. [9] is approximately 0.03–0.04), surface sand particles began to move by rolling and saltation, and a pit gradually formed at the toe; in this stage, the earth pressure of AI1-4 fluctuated slightly, showing that the formation of a scour hole does not equal internal stress instability. Stage 2 (scour expansion and toe instability): from about 70 s, the compressive stress of AI1-4 increased rapidly, reaching a peak compressive stress of −6.17 kPa at about 79 s, corresponding to the concentrated stage of rapid toe undercutting and local collapse, consistent with the cantilever failure mechanism of bank scour described by Simon et al. Stage 3 (progressive collapse and failure surface extension): after collapse, the failure surface propagated toward the slope interior and crest, and tensile cracks gradually appeared at the crest. Stage 4 (scour-hole stabilization and residual transport): sediment was continuously transported, and AI1-13 began to respond clearly at about 475 s; the post-test photos recorded complete toe undercutting, degradation of the slope surface into an irregular erosion profile, and multiple tensile cracks at the crest (Figure 6).



Figure 6. Post-test photographs of G1 (unprotected): complete toe undercutting and multiple tensile cracks.

The stress of AI1-4 reached its peak of −6.17 kPa (compressive stress) at about 79 s, with a peak-to-peak value of 6.99 kPa and a standard deviation of 2.13 kPa, both the highest of all conditions, and a skewness of −0.44 (left-skewed), indicating that the soil was continuously subjected to flow impact and compression by the collapsing soil mass. Apart from AI1-4, the peak-to-peak values of all other sensors were below 0.5 kPa (less than 6% of that of AI1-4), showing that the mechanical influence of scour was highly localized. The peak-to-peak value of AI1-9 was only 0.03 kPa, forming an approximately 230-fold contrast with the 6.99 kPa of AI1-4; the large response reflects internal scour and force-chain breakage, whereas the small response reflects only surface sand erosion. The response ratio of AI1-9 to AI1-4 of about 0.0043 (about 1/230) can be defined as a dimensionless

mechanical criterion for distinguishing surface scour from internal erosion. The peak-to-peak value of AI1-13 was 0.40 kPa; those of AI1-15 and AI1-16 were about 0.09 and 0.41 kPa, respectively, and those of the reference sensors AI1-1 to AI1-3 were below 0.01 kPa throughout. The representative time-history curves are shown in Figure 7.

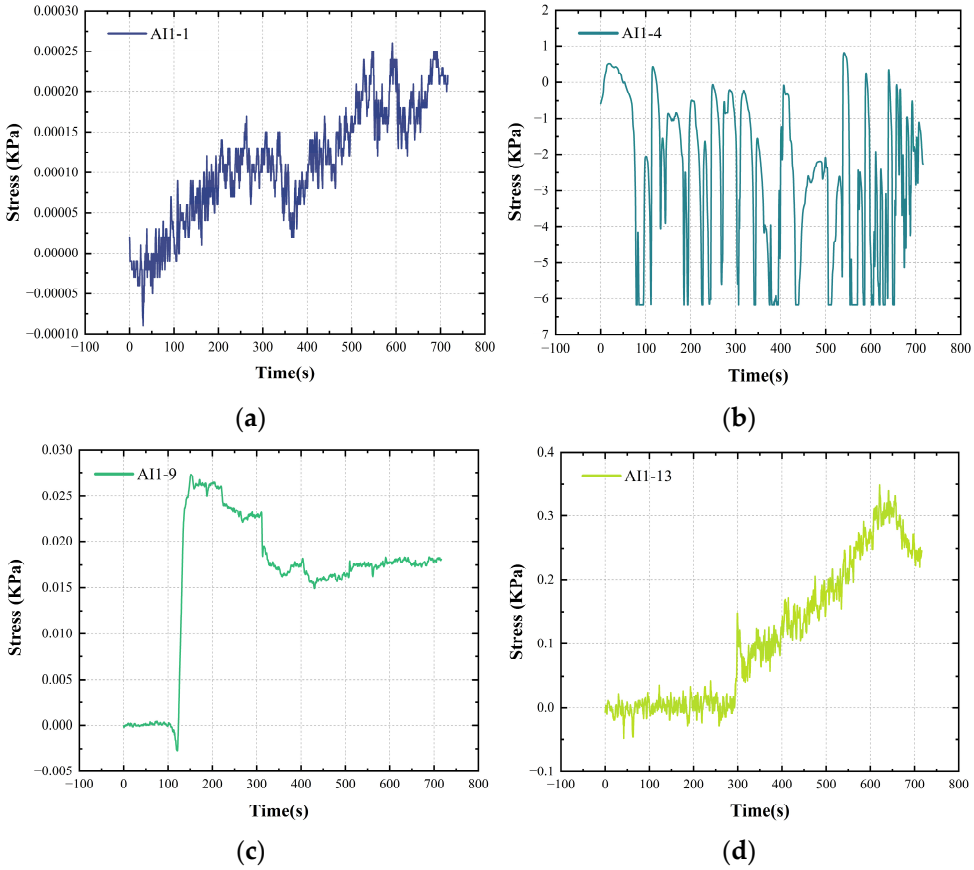


Figure 7. Representative time-history curves of G1 (unprotected, v = 0.2 m/s): (**a**) AI1-1 (reference) (**b**) AI1-4 (core sensor); (**c**) AI1-9 (surface erosion); (**d**) AI1-13 (early-warning).

In the unprotected configuration, failure began with progressive scour of the downstream toe. Initial small-scale particle displacement gradually evolved into surface erosion, and then clearly transformed into a cantilever collapse formation stage. This pattern is consistent with the overtopping failure results of non-cohesive slopes; the failure process generally develops from progressive toe erosion to sudden overall collapse.

3.2.2. Semi-Protected Subgrade Series (G2, G3)

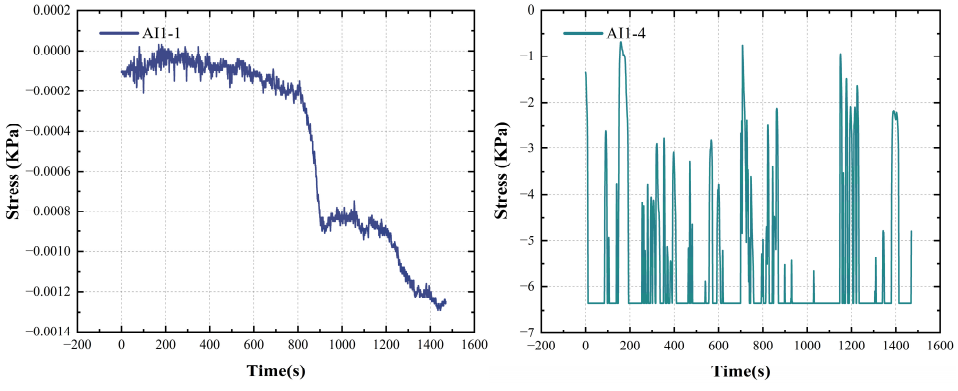
The semi-protected subgrade exhibits a more complex failure mechanism under the dual influence of structural constraint and hydraulic action. At 0.2 m/s (G2), the slope remained stable throughout. G2 lasted 1470.5 s, and the post-test photos show that the gabion had no displacement or deformation and the slope surface was intact (Figure 8). The peak-to-peak value of AI1-4 dropped to 5.66 kPa (a 19% reduction), and the standard deviation dropped to 1.49 kPa (a 30% reduction), corresponding to an approximately 30% reduction in turbulent-fluctuation amplitude by the gabion, consistent with the assessment of Freeman [14] that gabion gravel fill dissipates energy through collision and friction. The 19% reduction in the peak-to-peak value is difficult to reliably distinguish stability from failure under actual monitoring noise, which highlights the irreplaceable value of skewness; the skewness of G1 is −0.44 (left-skewed, with occasional large compressive stress spikes), whereas that of G2 reverses to +1.73 (right-skewed, sustained stable compression). The self-

weight of the gabion (equivalent density 1.6–1.8 g/cm3) applies a sustained preload to the underlying soil, transforming the soil from a loose, flow-impacted state into a continuously compressed, stable state, an independent mechanical effect of the gabion in addition to energy-dissipating filtering.



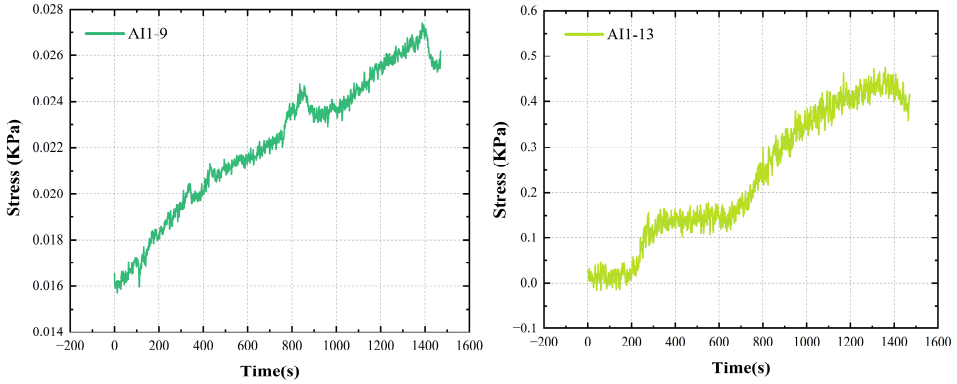
Figure 8. Post-test photographs of G2 (semi-protected, v = 0.2 m/s): intact slope surface and no gabion displacement.

G2, using 3–5 mm gravel and the steel wire mesh constraint, systematically avoids the problem of cushion particles being lost through gaps between riprap stones. AI1-10 dropped from 0.26 to 0.03 kPa (an 88% reduction), nearly dormant, indicating that the gabion significantly suppressed the flow disturbance there; whereas AI1-13 had a peak-to-peak value of about 0.49 kPa, slightly higher than the 0.40 kPa of G1. This is a direct manifestation of the weight-stabilizing effect of the gabion self-weight; the sustained preload applied by the cage weight to the underlying soil slightly elevates the stress of the sensor immediately below the cage, but its skewness has changed from left-skewed to right-skewed (see the aforementioned skewness reversal), which is self-consistent with the mechanical mechanism of weight stabilization. The gabion protection also has a neglected indirect effect: the high-porosity revetment does not prevent the transmission of dynamic water pressure into the deep soil, and seepage weakening reduces the effective stress. This constitutes two complementary driving mechanisms of scour failure: surface drag removing particles [9] and seepage force reducing internal strength [21]. The seepage weakening observed in G2 is exactly the precondition for piping to develop into G3 failure at high velocity. The representative time-history curves of G2 are shown in Figure 9, in which the magnitude difference between AI1-4 and the other sensors is clearly visible.



(**a**) (**b**)

Figure 9. *Cont.*



(**c**) (**d**)

Figure 9. Representative time-history curves of G2 (semi-protected, v = 0.2 m/s): (**a**) AI1-1 (reference); (**b**) AI1-4 (core sensor); (**c**) AI1-9 (surface erosion); (**d**) AI1-13 (early-warning).

At 0.4 m/s (G3), the failure mechanism evolved into a composite failure of piping and geotextile lifting. G3 failed after 1955.5 s. After the velocity increased to 0.4 m/s, the hydrodynamic drag increased by about four times (consistent with quadratic drag scaling, $(0.4/0.2)^2 = 4$); fine sand penetrated the gabion mesh to form piping, the geotextile locally lost support and lifted into wrinkles, and water flowed into the basal gaps to accelerate scour. The post-test photos record the wrinkled lifting zone of the geotextile and the cavity-like hollowed space below, a state that is externally intact but internally hollowed, which is extremely dangerous in engineering (Figure 10).



Figure 10. Post-test photographs of G3 (semi-protected, v = 0.4 m/s): geotextile lifting and cavity below.

The peak-to-peak value of AI1-4 jumped to 7.82 kPa (+38.2%). The peak-to-peak value of AI1-13 surged from 0.49 kPa in G2 to 1.02 kPa (+108%), an increase far exceeding that of AI1-4 and exceeding 1 kPa for the first time, with the response continuing to increase as failure developed; AI1-13 was thus identified as a candidate early-warning sensor (its threshold remains preliminary; Section 3.5). The jumps of AI1-12 (+433%) and AI1-10 (+3200%) verified the rapid bottom-up transmission of the failure signal. The peak-to-peak value of AI1-7 jumped by +1100%, verifying the spatial expansion mechanism of the internal erosion channel from the internal mechanical dimension. The representative time-history curves of G3 are shown in Figure 11.

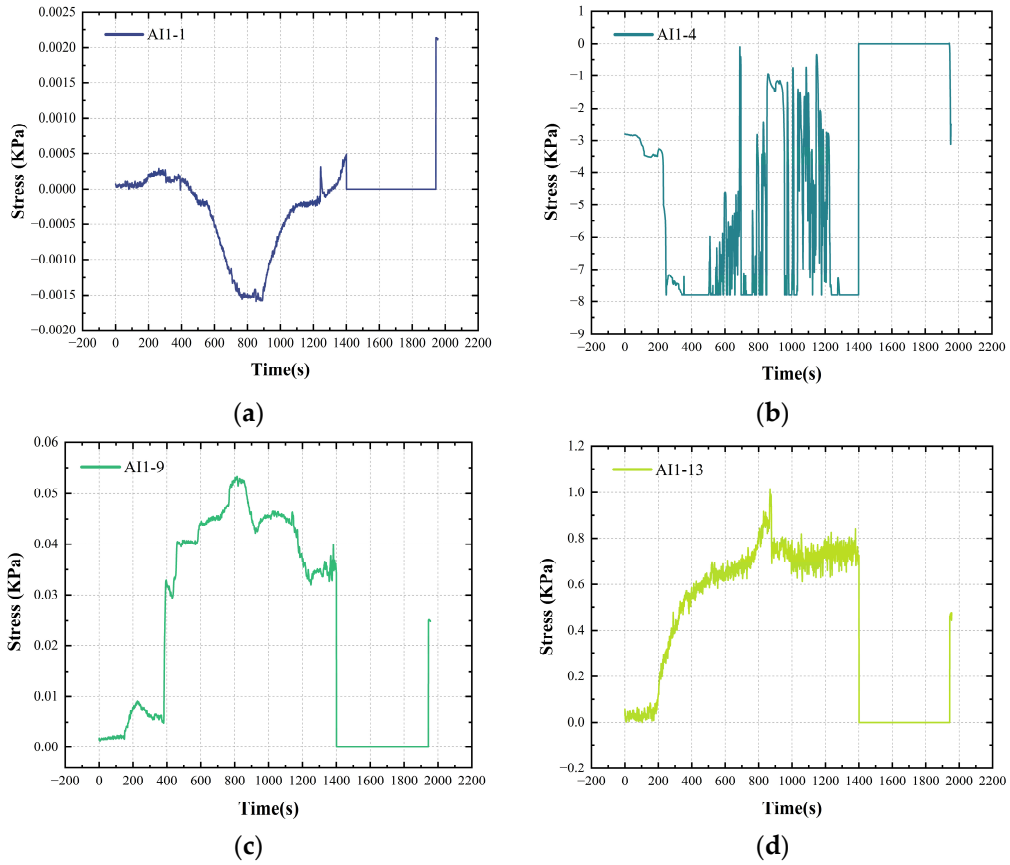


Figure 11. Representative time-history curves of G3 (semi-protected, v = 0.4 m/s): (**a**) AI1-1 (reference); (**b**) AI1-4 (core sensor); (**c**) AI1-9 (surface erosion); (**d**) AI1-13 (early-warning).

3.2.3. Fully Protected Subgrade Series (G4, G5, G6)

The fully protected series exhibits a failure mechanism that shifts significantly with increasing velocity. At 0.2 m/s (G4), the slope was nearly absolutely stable. G4 lasted 2125.5 s, the longest of all, and the peak-to-peak value of AI1-4 was only 0.016 kPa, close to the sensor noise floor and two orders of magnitude lower than the 5.66 kPa of G2; the step-wise protection gain of spur dike flow diversion made the toe nearly static. The post-test photos show an intact slope body and slight deposition downstream of the spur dike, which is a direct manifestation of the extremely low velocity and near-zero sediment-carrying capacity in the recirculation zone (Figure 12). The representative time history curves of G4 are shown in Figure 13.



Figure 12. Post-test photographs of G4 (fully protected, v = 0.2 m/s): intact slope and slight deposition.

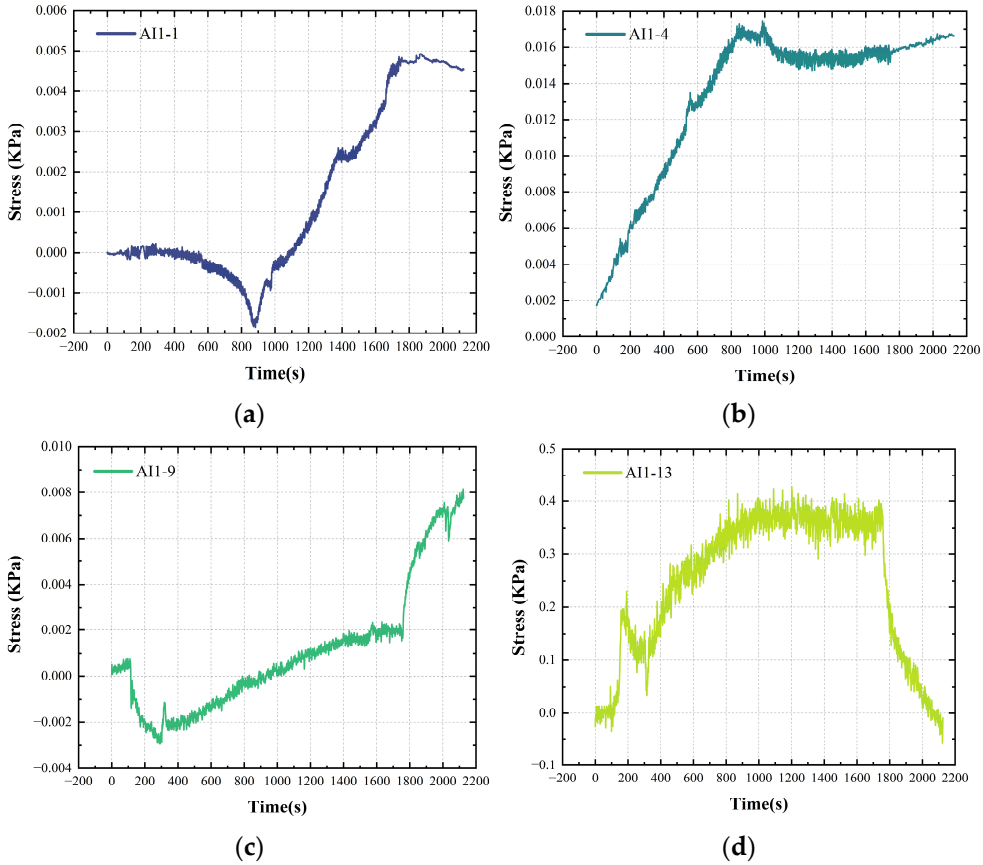


Figure 13. Representative time-history curves of G4 (fully protected, v = 0.2 m/s): (**a**) AI1-1 (reference); (**b**) AI1-4 (core sensor); (**c**) AI1-9 (surface erosion); (**d**) AI1-13 (early-warning).

At 0.4 m/s (G5), the slope was stable but exhibited a load-transfer mechanism. G5 lasted 1067 s and remained stable, with a peak-to-peak value of 13.07 kPa for AI1-4, the highest of all conditions (1.67 times that of the failed G3). This counterintuitive phenomenon of greater stress with more protection reveals the load-transfer mechanism: after spur dike flow diversion, the high-velocity main flow impacts the spur dike and gabion structures, and the drag force is transmitted downward and recorded as high-amplitude compressive stress, whereas the toe soil is barely directly affected by the flow because it lies in the hydrodynamic shadow zone; 13.07 kPa reflects the load carried by the protection structure rather than the soil being scoured. This active strategy of diverting flow to guide energy in G5 is fundamentally different from the passive strategy of sacrificing the outer riprap layer in Gao et al. [19]. The post-test photos show an intact slope body and increased deposition downstream of the spur dike (Figure 14). The representative time-history curves of G5 are shown in Figure 15.

At 0.8 m/s (G6), the slope exhibited ultimate failure accompanied by predictable mechanical precursors. G6 failed after only 626.5 s, with a failure sequence of spur dike resonant vibration, foundation scour, displacement of about 5 cm, failure of flow diversion, main flow impact on the gabion, gravel loss, and rapid toe scour. The post-test photos record the most severe failure morphology: obvious spur dike displacement and exposed steel wire mesh (Figure 16). The representative time-history curves of G6 are shown in Figure 17.



Figure 14. Post-test photographs of G5 (fully protected, v = 0.4 m/s): intact slope and increased deposition.

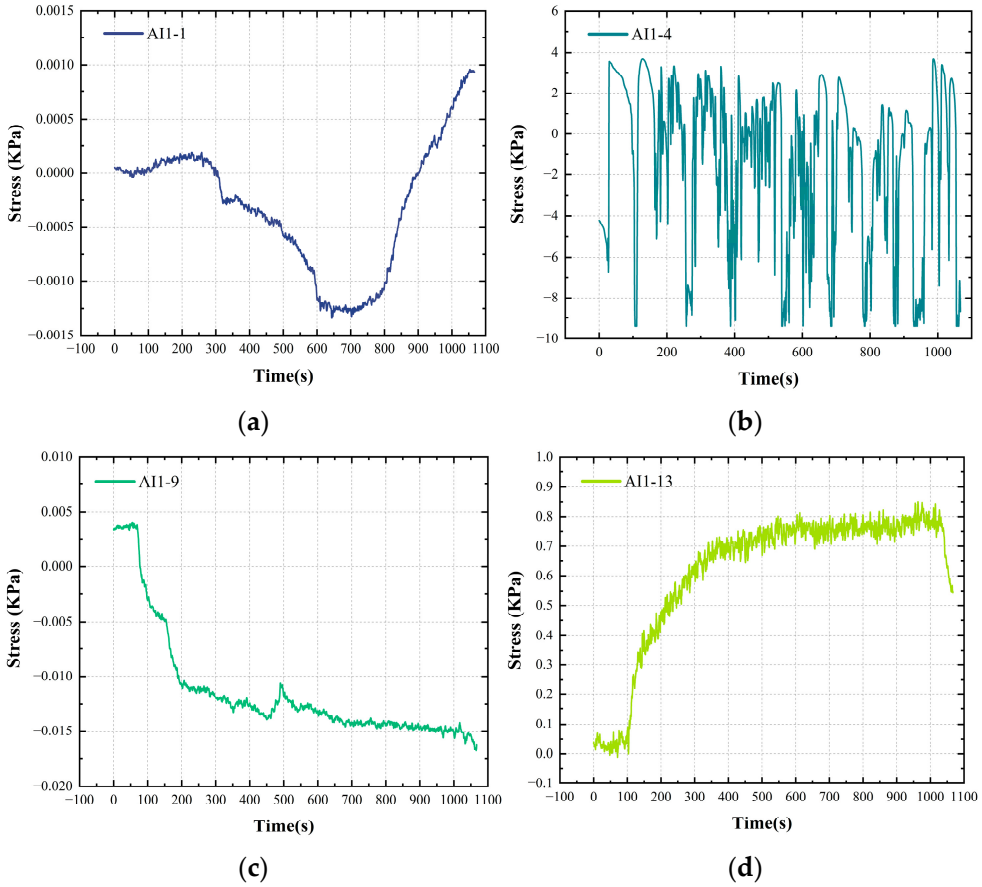


Figure 15. Representative time-history curves of G5 (fully protected, v = 0.4 m/s): (**a**) AI1-1 (reference); (**b**) AI1-4 (core sensor); (**c**) AI1-9 (surface erosion); (**d**) AI1-13 (early-warning).

The peak-to-peak value of AI1-4 was 11.98 kPa, 8.3% lower than that of G5, showing a rise-then-fall trend reversal. Within 2–4 min before failure, AI1-9, AI1-13, and AI1-17 simultaneously captured a stress drop synchronous with AI1-4; the three sensors provide mutually corroborating evidence (they are spatially distributed channels within a single test, not statistically independent replicates). The skewness further increased negatively, forming a dual mechanical warning signal with the peak-to-peak reversal (Figure 18). The drop in the peak-to-peak value indicates the progressive disappearance of the load-bearing medium (soil) beneath the protection structure, and the skewness turning negative indicates

that, after soil removal, the sensor membrane loses soil support and is directly exposed to flow action.



Figure 16. Post-test photographs of G6 (fully protected, v = 0.8 m/s): spur dike displacement and exposed wire mesh.

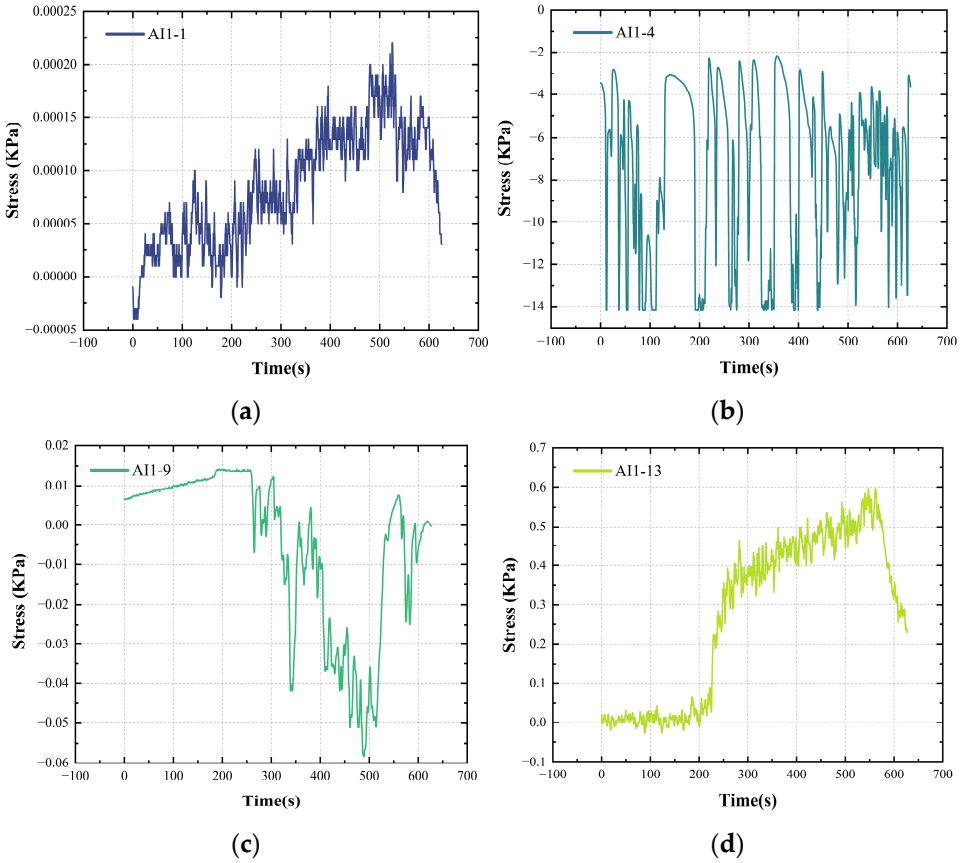


Figure 17. Representative time-history curves of G6 (fully protected, v = 0.8 m/s): (**a**) AI1-1 (reference); (**b**) AI1-4 (core sensor); (**c**) AI1-9 (surface erosion); (**d**) AI1-13 (early-warning).

The results of the fully protected series show that the failure mechanism shifts significantly with increasing velocity. At low velocity (G4), spur dike flow diversion makes the toe nearly absolutely stable; at medium velocity (G5), the protection structure transforms flow impact into structural load through the load-transfer mechanism, and the soil itself remains stable; at high velocity (G6), after the weakest link of the protection system is breached, failure unfolds rapidly with predictable mechanical precursor signals.

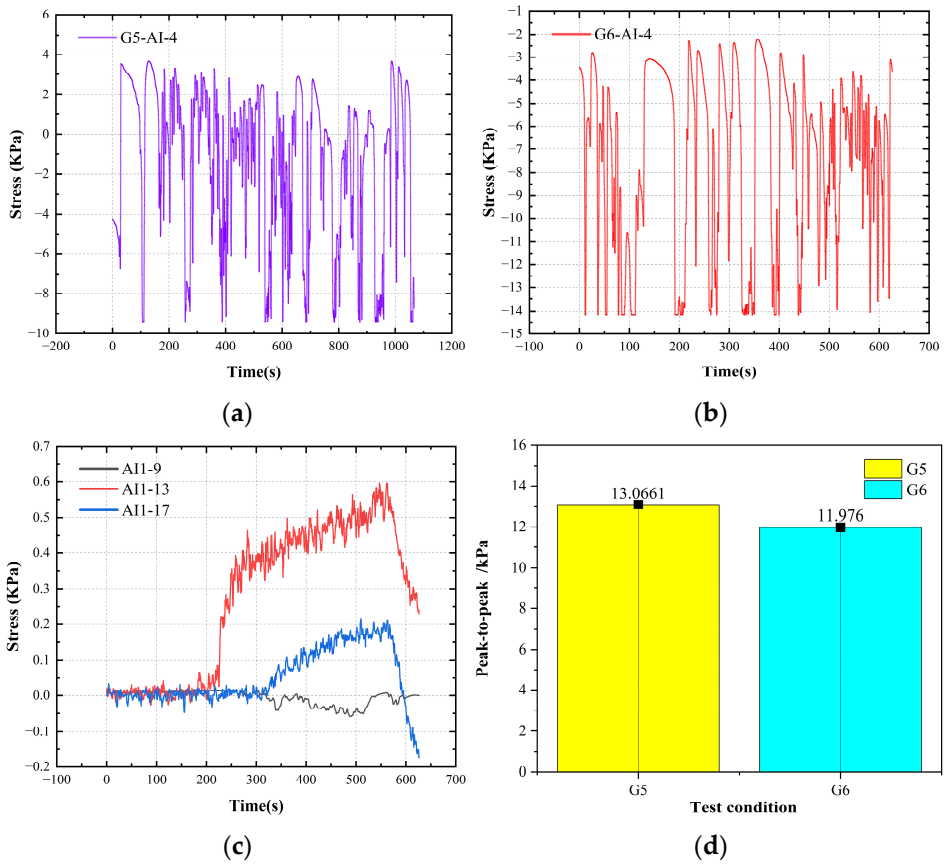


Figure 18. Dual mechanical warning signal of G6: (**a**) AI1-4 time history in G5 (**b**) AI1-4 time history in G6 (**c**) synchronous stress drop of AI1-9, AI1-13, and AI1-17 before failure (**d**) peak-to-peak values of AI1-4 in G5 and G6 (rise-then-fall, −8.3%).

3.3. Seepage Effects on the Failure Mechanism

In the unprotected case (G1), seepage exhibits a relatively uniform flow path from the toe to the crest. Because there are no structural obstacles, the water pressure can uniformly and continuously permeate the entire slope body, thereby intensifying the erosion at the toe. Seepage first appears at the toe (the zone where the water pressure is concentrated), thereby inducing local cutting; as the seepage line moves upward, the cutting effect gradually advances upslope, forming a step-wise progressive failure mode. Observations show that, before substantial slope displacement occurs, seepage has already appeared and intensified along the slope, causing soil particle detachment at the toe. This phenomenon is consistent with the results of bank seepage studies: upward seepage is inferred to reduce the effective stress and lower the critical shear threshold, thereby triggering earlier sediment motion (pore-water pressure was not directly measured in this study; this inference follows the bank-seepage literature). The coupling of seepage and surface scour indicates that riverside subgrade failure is a combined surface–subsurface erosion process rather than a purely hydraulic surface phenomenon. This interpretation is consistent with coupled seepage–stability analyses of earth-fill dams under rapid reservoir drawdown [27,28], in which transient seepage under rapid hydraulic loading likewise governs failure initiation.

In contrast, the protection structures in the protected configurations significantly alter the seepage dynamics. The structural design of the protection bodies breaks the uniform seepage state observed in the unprotected configuration, causing the seepage flow to form concentrated jets in the protection gaps and beneath the foundation. As in the unprotected case, seepage always starts from the toe; however, in the protected configurations, seepage is transmitted through the protection gaps, causing a sharp rise in seepage pressure in

specific zones (inferred, not directly measured). These concentrated flows form local jets that accelerate local scour and intensify erosion between the protection gaps. In condition G3, this mechanism is particularly evident: seepage forms concentrated channels through the gabion mesh and geotextile gaps, directly causing piping and geotextile lifting, and is precisely captured by the internal stress signal at AI1-7, verifying the spatial expansion path of the seepage channel from the internal mechanical dimension. At higher velocities, the seepage effect becomes more significant and further amplifies the local scour between protection gaps; seepage not only intensifies toe erosion but also induces vertical erosion through the formation of concentrated jets. Therefore, in embankments with protection structures, seepage acts as a local hydraulic driving factor that further intensifies erosion and slope collapse through concentrated jets and scour between protection gaps.

3.4. Mechanical Response Time-History Characteristics

The earth pressure time histories of the six tests all exhibit a generally consistent pattern of mechanical response evolution, including distinct initiation, acceleration, and attenuation stages that directly determine the slope failure behavior. Analysis of the response time histories reveals three clear stages: (1) gradual rise during the early stage of erosion; (2) sharp acceleration associated with scour expansion; and (3) attenuation after the scour hole enlarges and stabilizes. This initiation–acceleration–attenuation characteristic curve is highly consistent with the hydrograph of large-scale breaching; the peak stress corresponds to the maximum scour rate, followed by progressive recession, highlighting the transferability of failure theory to the riverside subgrade field.

In the initiation stage, as the flow acts on the toe, the earth pressure gradually rises. In low-velocity conditions such as G1 and G2, this stage lasts longer, and the earth pressure curve shows a slow linear rising trend, reflecting the formation of a stable mechanical state before scour. In contrast, in high-velocity conditions such as G3 and G6, the earth pressure rises rapidly in the initial stage, causing premature toe instability and rapid scour. These conditions embody an aggressive hydraulic initiation characteristic: the high velocity quickly exceeds the structural resistance of the slope.

The acceleration stage coincides with scour expansion, during which the earth pressure rises sharply and induces structural collapse. In most conditions, this stage presents a single dominant peak that coincides with intense erosion and the onset of failure. However, in G3, a more complex mechanical response is observed: two distinct peaks appear not in the initial acceleration stage but in the second half of the event, which is usually regarded as the attenuation stage. The first peak corresponds to the onset of piping and the beginning of mid-slope collapse; as the failure surface partially forms and stress redistributes, the earth pressure briefly drops. A second, more significant peak (corresponding to the +108% jump of AI1-13) then appears, induced by the formation of the mid-slope slip surface, causing stress concentration and steepening of the slip gradient; this peak coincides with a new stage of slope failure, fully demonstrating that even under unchanged hydraulic conditions, the reconfiguration of the failure surface geometry can trigger a rebound in the mechanical response.

Finally, the attenuation stage corresponds to the stabilization of the flow and structure, characterized by a plateau in the earth pressure and the cessation of major deformation. The stress level in this stage depends on the prevailing velocity intensity: under high-velocity conditions, the residual hydraulic energy can sustain particle transport, whereas under low-velocity conditions, the stress is almost negligible. It is noteworthy that the attenuation stage of G6 does not show a gradual decline; instead, the peak-to-peak value drops by 8.3% and is accompanied by a skewness reversal, constituting the dual mechanical warning signal before failure. These results jointly indicate that the attenuation of the mechanical

response during failure is not uniformly smooth; stress re-accumulation after collapse can trigger a secondary surge, especially when the evolution of the failure morphology alters the flow path and energy dissipation.

3.5. Higher-Order Statistical Characteristics and Protection Mechanism Criteria

To evaluate the evolution of the mechanical state of the subgrade during scour, statistical moments such as skewness (third moment) and standard deviation (second moment) were introduced in addition to the peak-to-peak value, revealing the protection mechanism from the two orthogonal dimensions of load distribution shape and energy fluctuation. The analysis results show that skewness, as a higher-order discriminant, can capture mechanical state transitions that amplitude parameters cannot identify.

In the unprotected G1, the skewness of AI1-4 is −0.44 (left-skewed) with a standard deviation of 2.13 kPa, indicating that the soil is continuously subjected to flow impact and that the load distribution is left-skewed. In the semi-protected G2, the skewness reverses to +1.73 (right-skewed) and the standard deviation drops to 1.49 kPa. This statistical reversal reveals, in terms of load distribution shape, the mechanical essence of the weight-stabilizing effect of the gabion: the self-weight of the gabion applies a sustained preload to the underlying soil, transforming the mechanical state of the soil from loose and flow-impacted to continuously compressed and stable. The 19% reduction in the peak-to-peak value is insufficient to reliably distinguish the two states, whereas the sign reversal of skewness provides a complementary discriminant. The sign of skewness alone, however, does not map one-to-one onto stability: the stable conditions G4 (−1.38) and G5 (−0.77) also show negative skewness, and the failed condition G3 shows near-zero skewness (+0.02). Skewness must therefore be interpreted jointly with the peak-to-peak amplitude and the sensor position (Section 3.5, Table 5) and is best regarded as a qualitative indicator of asymmetric stress release rather than a validated quantitative threshold.

Table 5. Key statistical indicators of AI1-4 and the three-level early-warning criteria for each condition.

Condition	Peak-to-Peak (kPa)	Skewness	Result	Key Finding
G1	6.99	−0.44	Failure	Compressive stress spike; first quantitative baseline
G2	5.66	+1.73	Stable	Skewness reversal: weight-stabilizing effect
G3	7.82	+0.02	Failure	Mid-slope sensitivity higher than toe
G4	0.016	−1.38	Stable	Spur dike diversion makes toe nearly static
G5	13.07	−0.77	Stable	Load transfer: high stress means high safety
G6	11.98	−0.56	Failure	Rise-then-fall + skewness reversal dual warning

Notes: Three-level early-warning criteria (tentative, derived from non-replicated tests, based on the combined AI1-4 and AI1-13 dual-sensor criterion). Because skewness is physically meaningful only when the sensor signal clearly exceeds the noise floor, it must be interpreted jointly with the peak-to-peak amplitude. ① Safe: the skewness reverses from negative to positive together with a reduced peak-to-peak value (weight-stabilized, e.g., G2); ② Alert: the peak-to-peak value rises abnormally, or the skewness turns negative from a positive baseline; ③ Danger: the peak-to-peak value rises then falls (an ~8.3% rise-then-fall reversal, as observed in G6) while the skewness turns negative (dual mechanical warning signal, e.g., G6).

In the fully protected G6, the skewness further increases negatively (<−0.44), which, together with the rise-then-fall of the peak-to-peak value (−8.3%), constitutes a dual mechanical precursor observed in this test. The skewness turning negative means that, after soil removal, the sensor membrane loses soil support and is directly exposed to flow action, i.e., the disappearance of the load-bearing medium; the drop in the peak-to-peak

value means stress unloading of the soil beneath the protection structure. The two jointly indicate the imminent failure from different dimensions.

It should be noted that the skewness is physically meaningful only when the sensor signal clearly exceeds the noise floor. In the near-static condition G4 (−1.38) and the load-transfer condition G5 (−0.77), the skewness is dominated by noise and by the transferred structural load, respectively, and both are negative despite the conditions being stable; the sign of skewness therefore does not by itself indicate stability or failure, and it must be interpreted jointly with the peak-to-peak amplitude and the sensor position (Table 5).

4. Discussion

4.1. Failure Stages of Riverside Subgrade Scour

Based on the experimental evidence, the scour failure process of riverside highway subgrades can be summarized into four stages: (1) initial flow establishment and seepage onset; (2) scour expansion and toe instability; (3) progressive collapse and failure surface extension; and (4) scour-hole stabilization with residual sediment transport. These stages appear consistently in all test conditions, regardless of protection level or flow velocity. Although the intensity and complexity of each stage differ, the overall development process remains consistent, providing a general framework for understanding the evolution of riverside subgrade scour failure. This staged pattern is highly consistent with the classical failure models established for slope and natural dam failure [29–31]. The stress time-history characteristics of each stage can be supported by the overview heatmap in Figure 5 and the time-history curves of the failure conditions (Figures 7, 13 and 17).

In the first stage, while the toe is directly acted upon by the flow, seepage gradually appears within the slope body and raises the pore pressure, weakening the stability of the slope base. This stage is usually accompanied by the appearance of toe displacement, marking the first obvious response of the structural system to hydraulic loading. It should be emphasized that the AI1-4 observed in this test fluctuated only slightly within ±1 kPa in the early stage of scour-hole formation, indicating that the formation of a visible scour hole is not equivalent to internal stress instability; this finding reveals a time-sequence characteristic in which the appearance precedes the instability in the failure process. The second stage begins when scour expansion develops to cantilever formation, and the hydraulic action mechanism changes from predominantly surface erosion to combined surface–subsurface action; this change triggers the first major structural failure, manifested as toe collapse or retrogressive erosion, the form of which depends on the flow intensity. The third stage is manifested as the upward expansion of the failure surface and further slope deformation; secondary failure mainly originates from the change in failure surface geometry; the flow turns toward newly exposed or weak zones of the slope, causing a significant increase in local shear stress and hydraulic gradient (especially on steep slopes), thereby accelerating erosion and destabilizing adjacent sections. The final stage marks the system reaching a mechanically and hydraulically stable state, characterized by the plateau of stress and the complete cessation of major deformation.

4.2. Influence of Hydraulic Action on Failure Mechanisms

The variation of mechanical response under different flow velocities provides important insights into how hydraulic action dominates the scour failure process of subgrades. Within the same protection level, the failure behavior shows a clear transition with increasing velocity. In the semi-protected series, 0.2 m/s (G2) remained stable throughout, whereas 0.4 m/s (G3) experienced multi-phase failure of piping initiation and mid-slope slip surface formation, with the stress curve showing two distinct peaks (corresponding to piping initiation and mid-slope slip surface formation, respectively); in the fully protected

series, 0.2 m/s (G4) was nearly static, 0.4 m/s (G5) was stable but exhibited load transfer, and 0.8 m/s (G6) failed rapidly, with the stress rising quickly followed by a rise-then-fall reversal and then entering the warning stage. It should be noted that the duration of G3 (0.4 m/s, semi-protected) of 1955.5 s is longer than the 716.5 s of G1 (0.2 m/s, unprotected); this difference mainly originates from the different protection levels rather than a velocity effect; the influence of velocity on the failure process should be compared within the same protection level.

These results show that, within the same protection level, increasing the velocity shortens the duration of each failure stage and increases the stress amplitude, thereby promoting the transition from progressive scour to rapid retrogressive failure. The experimental results highlight the significant influence of hydraulic loading on both the time course and morphology of failure development in submerged riverside subgrades: at low velocities, failure mainly manifests as progressive toe scour, whereas high velocities lead to rapid retrogressive erosion and more abrupt slope collapse. Similar phenomena have been reported in flume tests of non-cohesive slopes; high discharge accelerates failure surface expansion and forms step-wise erosion features [32].

Further analysis shows that the three stages of mechanical response (initiation, acceleration, and attenuation) are closely related to but not completely identical with the structural failure stages. In the initiation stage, the stress gradually rises, particle motion is weak, and only slight toe erosion or local deformation occurs, corresponding to the early failure stage of initial flow development and seepage formation; when the system enters the acceleration stage, both stress and deformation intensify significantly, corresponding to the scour expansion and toe instability stage; subsequently, in the attenuation stage, the stress gradually stabilizes, corresponding to the scour-hole stabilization and residual transport period, during which active deformation stops but sediment transport may persist (especially under high-velocity conditions).

Based on three discrete velocities and single (non-replicated) runs, the data indicate broad transition intervals rather than precise critical velocities. The unprotected system failed at 0.2 m/s; the semi-protected system remained stable at 0.2 m/s and failed at 0.4 m/s; and the fully protected system remained stable up to 0.4 m/s and failed at 0.8 m/s (prototype 1.4, 2.8, and 5.7 m/s). These results are consistent with a cumulative increase of roughly four times in the threshold band of the three systems, but the exact critical velocities cannot be resolved from three velocity levels and should be treated as preliminary bounds (Section 2.3). The failure mode shifts systematically with the protection level, from direct toe scour, through piping and geotextile lifting, to spur dike displacement and flow-diversion failure, logically consistent with the failure sequence observed by Gao et al. [19]. The overview heatmap of all conditions is shown in Figure 5, and the time-history curves are shown in Figures 7, 9, 11, 13, 15 and 17.

The established three-level early-warning system (Table 5) is based on the combined dual-sensor criterion of AI1-4 and AI1-13, providing an experimental benchmark for the hierarchical configuration of protection systems and engineering early warning, transforming empirical selection into a preliminary, non-validated quantitative stratification. The four-statistic bar comparison of all 18 sensors is shown in Figure 19.

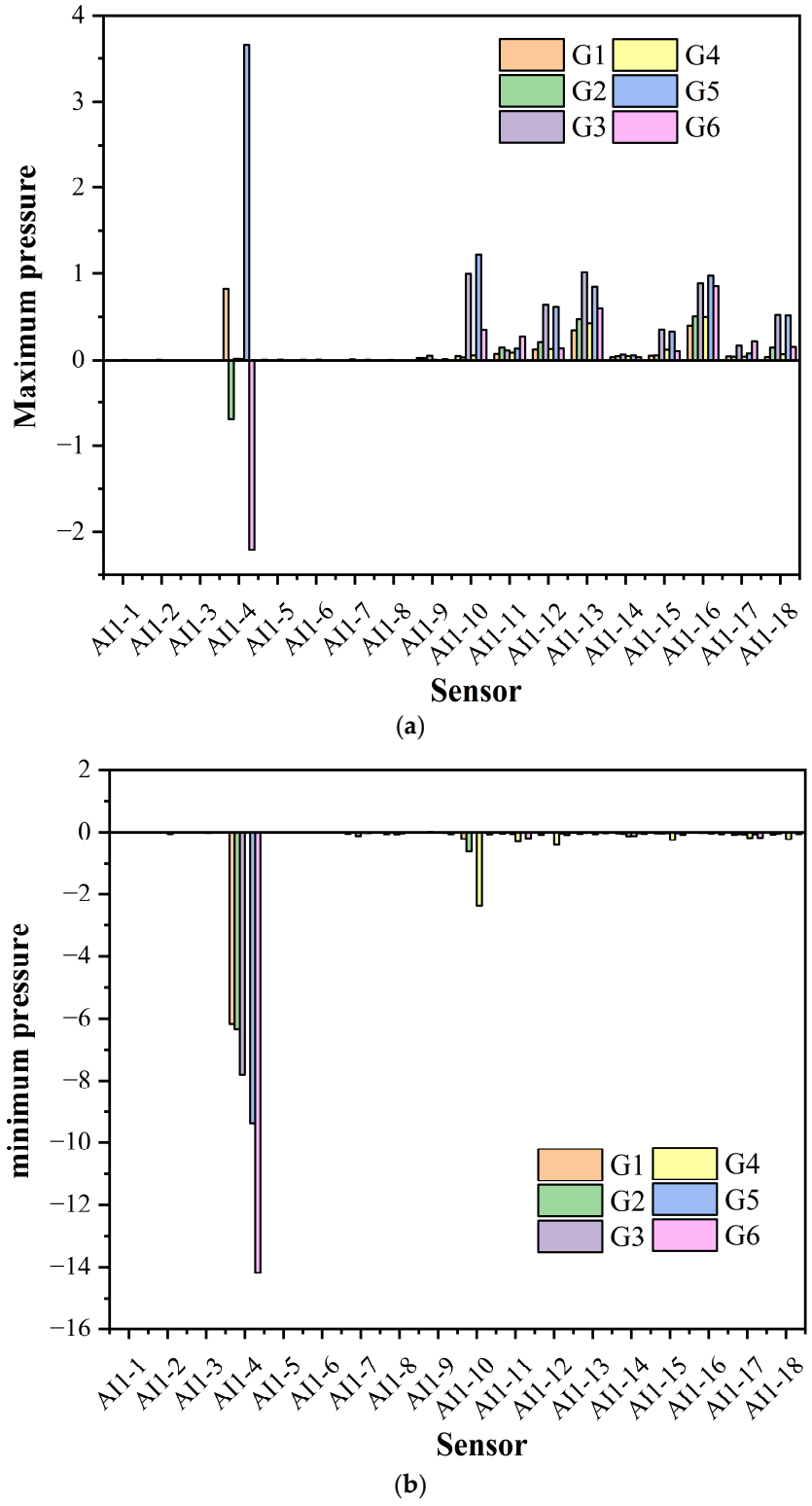


Figure 19. *Cont.*

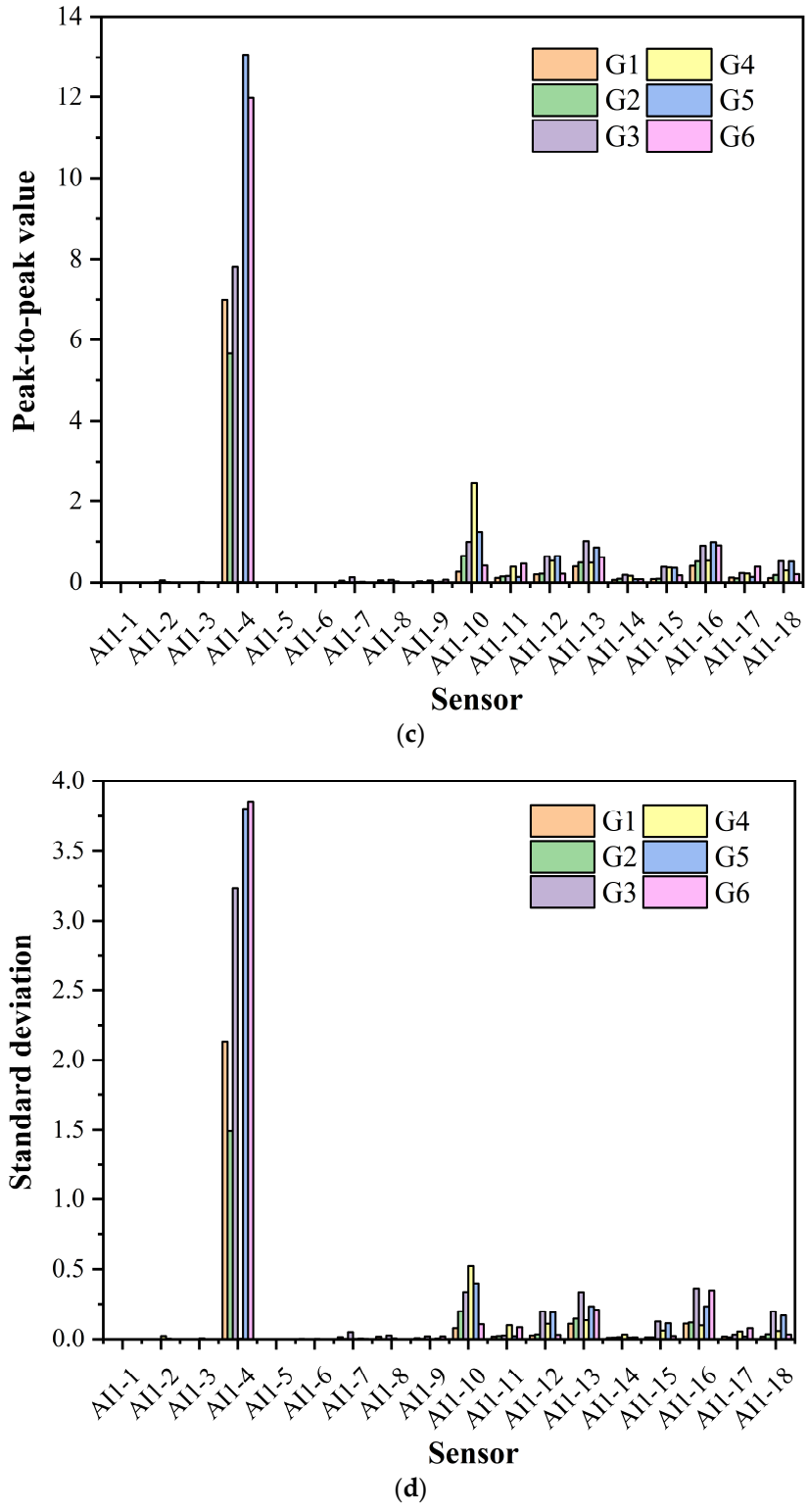


Figure 19. Comparison of four statistical indicators of the 18 sensors: (**a**) maximum pressure; (**b**) minimum pressure; (**c**) peak-to-peak value; (**d**) standard deviation.

4.3. Dual Effects of Protection on Failure Propagation

By comparing the mechanical responses of the unprotected, semi-protected, and fully protected cases at different velocity levels, it can be found that the presence of protection structures significantly affects the time-sequence characteristics and variation patterns of the failure process, and this influence exhibits a clear dual effect.

Under low-velocity conditions, the protection structures can provide temporary structural support, delay failure initiation, and regulate stress concentration, thereby promoting a slow and stable development of the failure process. In G2, the weight-stabilizing effect (skewness reversal from −0.44 to +1.73) and the energy-dissipating filtering effect (30% reduction in standard deviation) of the gabion act together, doubling the critical velocity of the semi-protected case compared with the unprotected case; in G4, spur dike flow diversion reduces the toe stress by another two orders of magnitude (AI1-4 only 0.016 kPa), achieving near-absolute stability.

However, under higher velocity conditions, the protection structures form localized high-velocity flow passages between themselves and the eroded slope, intensifying local scour and accelerating failure surface migration. The piping and geotextile lifting caused by concentrated seepage in the protection gaps in G3, and the rapid scour caused by the main flow directly impacting the gabion after the spur dike is breached in G6, both reflect this negative effect. This characteristic highlights both the role of protection structures in improving scour resistance in low-velocity events and their potential to intensify the failure mechanism under higher hydraulic loading through the formation of spatially heterogeneous flow patterns.

These results confirm that the presence of protection structures significantly alters the hydraulic flow path. Concentrated overflow at the protection gaps induces local scour and accelerates slope failure. This phenomenon is consistent with the results of heterogeneous subgrade tests; structural differences, such as coarse-grained cover layers, can lead to asymmetric failure surface expansion. Therefore, in the design of riverside subgrade protection, although protection structures are crucial for subgrade stability, their presence can also introduce hydraulic vulnerability during overflow; this dual effect must be fully considered when designing scour-resistant riverside subgrades and interpreting the results of physical model tests involving protection configurations.

4.4. Limitations

Although the physical model tests in this study provide valuable insights into the failure mechanisms of riverside subgrades under controlled scour conditions, several limitations must be acknowledged. First, the experimental design is based on scaled flume tests to simulate the scour and failure development process. Although Froude similarity was maintained through a 1:50 geometric scale, the scale effects detailed in Section 2.3 (hydraulic roughness, particle interaction, sediment-transport thresholds, seepage time scale, and geotextile/wire-mesh stiffness) mean that the model may not fully reproduce prototype behavior. Scaled embankments are weaker than prototypes because they lack the cohesion component, and the critical velocity obtained in this test is somewhat conservative when extrapolated to the prototype. Although these factors do not change the basic physical mechanisms governing subgrade deformation and failure development, the results should be regarded as representative conclusions reflecting the core physical behavior and interaction mechanisms of full-scale subgrades, rather than direct quantitative predictions.

Second, the specified hydraulic conditions are idealized as constant inflow velocity and do not reflect the fluctuating characteristics of actual flood hydrographs (dynamic rising and falling limbs, variable sediment inflow, and complex boundary conditions). In addition, the model adopts a uniform slope shape and homogeneous fill, without considering the spatial variability of natural soil; the incompatibility of Froude and Reynolds similarity leads to amplified viscous effects; the velocity range is limited to 0.2–0.8 m/s and does not cover higher extreme velocity intervals; and the effects of vegetation root reinforcement [33] and complex geometric boundary configurations such as wing-wall corners [19] are not addressed. Future research can overcome these limitations by introducing unsteady flow

fields, full-scale tests, or numerical simulation methods, thereby improving the applicability in real infrastructure systems.

Third, scour is a destructive and irreversible process, and each condition was tested only once without strict repeated tests. To support the reliability of the data, this study provides three guarantees: first, multiple measurement points corroborate each other, constituting spatial repetition; second, the failure/stability judgments of the six conditions are consistent with the progressive trends of velocity and protection level (G1, G3, G6 failed; G2, G4, G5 stable), with coherent cross-condition patterns; third, the reference sensors AI1-1 to AI1-3 show readings below 0.01 kPa throughout, close to the sensor noise floor, indicating a stable acquisition system without obvious drift. Nevertheless, these spatial and cross-condition checks are not substitutes for independent physical replicates. Because the 288,000 readings are serially autocorrelated time-series observations from a single run per condition rather than independent samples, the effective sample size is governed by the number of tests and the temporal autocorrelation of the signals, not by the total number of readings; the standard deviations and skewness values in Table 5 are therefore temporal-signal statistics of single runs, not ensemble statistics of repeated trials. A formal autocorrelation, effective-sample-size, and confidence-interval analysis within a time-series framework is required before any of these values are interpreted as statistically established thresholds.

Fourth, several measurements required for a fully mechanistic interpretation were not performed in this exploratory test program: local flow velocity and turbulence (e.g., ADV/PIV), bed shear stress, and pore-water pressure were not recorded, and the scour-hole geometry was not surveyed continuously, so scour-depth evolution curves cannot be reconstructed from the present data. The seepage and hydrodynamic interpretations in Sections 3.3 and 3.4 are therefore partly inferential. Future work should add synchronous local-velocity and pore-pressure instrumentation and continuous bed-morphology tracking to close these gaps.

5. Conclusions

Using scaled physical models, this study simulated the flood scour failure of riverside highway subgrades under different hydraulic and protection-structure conditions and systematically investigated the failure mechanisms of flood-affected subgrades and the protective performance of multi-level protection systems. The main findings are summarized as follows:

(1) The reduced-scale physical modeling method reproduced the dominant failure mechanisms of riverside subgrades under flood conditions. The model accurately reproduced the complete evolution of subgrade scour failure, which consistently follows a unified stage sequence: initial flow establishment and seepage onset, scour expansion and toe instability, progressive collapse and failure surface extension, and scour-hole stabilization with residual sediment transport. The experimental results also reproduced both progressive toe scour and rapid retrogressive erosion at high velocities, demonstrating that reduced-scale physical modeling can capture the staged scour-failure sequence of riverside subgrades under different hydraulic conditions.

(2) For the first time, an 18-channel synchronous earth pressure acquisition system embedded along the slope was integrated inside a scaled subgrade model (≈288,000 readings, ≈16,000 synchronous samples), fully covering the stress decay gradient of more than 700 times from AI1-4 to the reference sensor AI1-1. The approximately 230-fold response ratio between AI1-9 and AI1-4 supports a preliminary mechanical criterion for distinguishing surface scour from internal erosion, supplementing the surface-erosion versus internal-erosion classification framework of Briaud with a quantitative identifi-

cation method based on internal stress monitoring. The finding in G1 that a visible scour hole does not equal internal stress instability could only be obtained through internal mechanical monitoring.

(3) Hydraulic intensity is the primary factor controlling the failure process. Within the same protection level, increasing the flow velocity significantly shortens the duration of the failure initiation and acceleration stages, leading to faster failure and higher stress peaks. The failure mode changes from progressive toe scour at low velocities to dynamic retrogressive erosion at high velocities, where more intense failure surface extension and sediment transport are observed.

(4) The presence of protection structures exerts a dual effect on failure dynamics. Under low-velocity conditions, they provide temporary structural support and delay failure and regulate stress concentration through weight stabilization (skewness reversal from −0.44 to +1.73) and energy-dissipating filtering (30% reduction in standard deviation); under high-velocity conditions, however, they form localized high-velocity flow passages between the structure and the eroded slope, intensifying local scour and accelerating failure surface migration. The failure chain of piping–geotextile lifting in G3 and the failure sequence of spur-dike displacement–flow diversion failure in G6 both reflect the negative effects of protection structures under high hydraulic loading.

(5) A higher-order statistical method for discriminating the mechanical state of protection systems was proposed. As a higher-order discriminant introduced into the field of scour protection research, skewness reveals protection mechanisms from the orthogonal dimension of load distribution shape that amplitude parameters cannot capture. The dual mechanical warning signal composed of the rise-then-fall of the peak-to-peak value (−8.3%) and the skewness reversal appeared 2–4 min before failure and was synchronously confirmed by three sensors, which is more direct than indirect hydraulic-parameter warnings.

(6) The threshold band of the three protection systems increased cumulatively by roughly four times (based on three discrete velocities; Section 4.2), and the failure mode shifted systematically with the protection level. A three-level early-warning system based on the combined AI1-4 and AI1-13 dual-sensor criterion was proposed, providing an experimental benchmark for the hierarchical configuration of protection systems and engineering early warning, transforming empirical selection into a preliminary, non-validated quantitative stratification.

Author Contributions: Conceptualization, W.G. and P.H.; methodology, W.G., P.H., and S.G.; software, W.G., P.H., and S.R.; validation, W.G., H.X., and S.Y.; formal analysis, W.G. and P.H.; investigation, W.G., P.H., H.X., and S.Y.; resources, S.G., H.X., and S.Y.; data curation, W.G. and S.R.; writing—original draft preparation, W.G. and P.H.; writing—review and editing, S.G., W.G., and P.H.; visualization, W.G. and S.R.; supervision, S.G.; project administration, S.G.; funding acquisition, S.G. All authors have read and agreed to the published version of the manuscript.

Funding: Opening Fund of the Central Government Guides Local Science and Technology Development Fund Project of Sichuan Province (2025ZYDF080) 2025 Hainan Provincial Natural Science Foundation for High-level Talents (425RC798).

Data Availability Statement: The original contributions presented in this study are included in the article. Further inquiries can be directed to the corresponding author.

Acknowledgments: During the preparation of this manuscript/study, the authors used DeepSeek-V4-Pro for the purposes of organizing and screening the experimental data. The authors have reviewed and edited the output and take full responsibility for the content of this publication.

Conflicts of Interest: Authors Haitao Xu and Shasha Yi were employed by the company Mianyang Chuanjiao Highway Planning, Survey and Design Co., Ltd., Mianyang, China. The remaining authors declare that the research was conducted in the absence of any commercial or financial relationships that could be construed as a potential conflict of interest.

References

1. Mallakpour, I.; Villarini, G. The changing nature of flooding across the central United States. *Nat. Clim. Change* **2015**, *5*, 250–254. [CrossRef]
2. Munoz, S.E.; Giosan, L.; Therrell, M.D.; Remo, J.W.; Shen, Z.; Sullivan, R.M.; Wiman, C.; O'Donnell, M.; Donnelly, J.P. Climatic control of Mississippi River flood hazard amplified by river engineering. *Nature* **2018**, *556*, 95–98. [CrossRef]
3. Pinter, N.; Jemberie, A.A.; Remo, J.W.F.; Heine, R.A.; Ickes, B.S. Flood trends and river engineering on the Mississippi River system. *Geophys. Res. Lett.* **2008**, *35*. [CrossRef]
4. Rinaldi, M.; Darby, S.E. 9 Modelling river-bank-erosion processes and mass failure mechanisms: Progress towards fully coupled simulations. *Dev. Earth Surf. Process.* **2007**, *11*, 213–239. [CrossRef]
5. Simon, A.; Curini, A.; Darby, S.E.; Langendoen, E.J. Bank and Near-bank Processes in an Incised Channel. *Geomorphology* **2000**, *35*, 193–217. [CrossRef]
6. Wutti, S.; Wongchana, P.; Jitsangiam, P.; Chaikla, K.; Bualuang, T.; Thienchai, C. Assessment of failure mechanisms for railway embankments due to ballast layer breaching under flooding conditions. *Eng. Fail. Anal.* **2025**, *185*, 110433. [CrossRef]
7. Briaud, J.-L.; Chen, H.-C.; Govindasamy, A.V.; Storesund, R. Levee Erosion by Overtopping in New Orleans during the Katrina Hurricane. *J. Geotech. Geoenvironmental Eng.* **2008**, *134*, 618–632. [CrossRef]
8. Briaud, J.-L.; Govindasamy Anand, V.; Shafii, I. Erosion Charts for Selected Geomaterials. *J. Geotech. Geoenvironmental Eng.* **2017**, *143*, 04017072. [CrossRef]
9. Briaud, J.L.; Ting, F.C.K.; Chen, H.C.; Cao, Y.; Han, S.W.; Kwak, K.W. Erosion Function Apparatus for Scour Rate Predictions. *J. Geotech. Geoenvironmental Eng.* **2001**, *127*, 105–113. [CrossRef]
10. Mohammadnezhad, H.; Mohammadi, M.; Ghaderi, A. Riprap mitigation of downstream scour at grade-control structures considering tailwater depth and layer thickness. *Sci. Rep.* **2026**, *16*, 6680. [CrossRef]
11. Ettema, R.; Bergendahl, B.S.; Yorozuya, A.; Idil-Bektur, P. Breaching of Bridge Abutments and Scour at Exposed Abutment Columns. *J. Hydraul. Eng.* **2016**, *142*, 06016010. [CrossRef]
12. Ettema, R.; Ng, K.; Chakradhar, R.; Fuller, J.; Kempema, E.W. Failure of Spill-Through Bridge Abutments during Scour: Flume and Field Observations. *J. Hydraul. Eng.* **2015**, *141*, 06015001. [CrossRef]
13. Idil-Bektur, P.; Ettema, R. Large-Flume Observations of Scour at Bridge Abutments with Weak Compacted-Soil Embankment Approaches. *J. Hydraul. Eng.* **2017**, *143*, 06017020. [CrossRef]
14. Freeman, G.E.; Fischenich, J.C. Gabions for Streambank Erosion Control. 2000. Available online: https://www.scribd.com/document/499186794/Gabions-for-Streambank-erosion-control (accessed on 20 August 2026).
15. Lagasse, P.F. *Riprap Design Criteria, Recommended Specifications, and Quality Control*; Transportation Research Board: Washington, DC, USA, 2006.
16. Melville, B.W.; van Ballegooy, S.; Coleman, S.E.; Barkdoll, B. Riprap Size Selection at Wing-Wall Abutments. *J. Hydraul. Eng.* **2007**, *133*, 1265–1269. [CrossRef]
17. Kuhnle, R.A.; Alonso, C.V.; Shields, F.D. Local Scour Associated with Angled Spur Dikes. *J. Hydraul. Eng.* **2002**, *128*, 1087–1093. [CrossRef]
18. Duan, J.G. Mean Flow and Turbulence around a Laboratory Spur Dike. *J. Hydraul. Eng.* **2009**, *135*, 803–811. [CrossRef]
19. Gao, K.; Naito, C.; Suleiman, M.T.; Weisman, R.; Carre, T. Erosion Mitigation of Bridge Abutment Backfill during Flood Events. *J. Perform. Constr. Facil.* **2023**, *37*, 04023054. [CrossRef]
20. Sherzai, J.H.; De Costa, R.; Tanaka, N. Effects of Roughness of an Embankment Slope or Application of a Geo-Grid or Moat on Scouring Phenomena Downstream of an Embankment. *Arab. J. Sci. Eng.* **2022**, *48*, 4769–4784. [CrossRef]
21. Qiu, H.; Yang, J.; Li, Y.; Liang, Y.; Zhu, Y.; Song, J. Cascading flood impacts of potential landslide dams revealed by InSAR and numerical simulation. *J. Hydrol.* **2026**, *679*, 136217. [CrossRef]
22. Wang, K.; Xie, L.; Xie, S.; Zhang, S.; Jiang, Y.; Zhang, J.; Zhu, L.; Wang, Z.; Qi, F. Constructing physical-based rainfall landslides prediction model: Insights from rainfall threshold curves database of slope units. *Nat. Hazards Earth Syst. Sci.* **2026**, *26*, 2367–2385. [CrossRef]
23. Chanson, H. *Environmental Hydraulics for Open Channel Flows*; Elsevier: Amsterdam, The Netherlands, 2004.
24. Heller, V. Scale effects in physical hydraulic engineering models. *J. Hydraul. Res.* **2011**, *49*, 293–306. [CrossRef]
25. Zhao, Y.; Yi, J.; Yao, R.; Li, F.; Hill, R.L.; Gerke, H.H. Dimensionality and scales of preferential flow in soils of Shale Hills hillslope simulated using HYDRUS. *Vadose Zone J.* **2024**, *23*, e20367. [CrossRef]

26. Tsubaki, R.; Kawahara, Y.; Ueda, Y. Railway embankment failure due to ballast layer breach caused by inundation flows. *Nat. Hazards* **2017**, *87*, 717–738. [CrossRef]
27. Ghaderi, A.; Nazari, F.; Mohammadnezhad, H. Hydro-Mechanical Response of an Earth-Fill Dam During Rapid Reservoir Drawdown Using Coupled Seepage and Stability Analysis. *Geotech. Geol. Eng.* **2026**, *44*, 187. [CrossRef]
28. Ghaderi, A.; Parvinshoar, A.; Mohammadnezhad, H. Coupled unsaturated flow and stability assessment of Mahabad earth-fill dam under variable drawdown rates. *Acta Geophys.* **2026**, *74*, 73. [CrossRef]
29. ASCE/EWRI Task Committee on Dam/Levee Breaching. Earthen Embankment Breaching. *J. Hydraul. Eng.* **2011**, *137*, 1549–1564. [CrossRef]
30. Jiang, X.; Wei, Y.; Wu, L.; Hu, K.; Zhu, Z.; Zou, Z.; Xiao, W. Laboratory experiments on failure characteristics of non-cohesive sediment natural dam in progressive failure mode. *Environ. Earth Sci.* **2019**, *78*, 538. [CrossRef]
31. Jiang, X.; Wörman, A.; Chen, P.; Huang, Q.; Chen, H. Mechanism of the progressive failure of non-cohesive natural dam slopes. *Geomorphology* **2020**, *363*, 107198. [CrossRef]
32. Walder, J.S.; Iverson, R.M.; Godt, J.W.; Logan, M.; Solovitz, S.A. Controls on the breach geometry and flood hydrograph during overtopping of noncohesive earthen dams. *Water Resour. Res.* **2015**, *51*, 6701–6724. [CrossRef]
33. Darby, S.E.; Rinaldi, M.; Dapporto, S. Coupled simulations of fluvial erosion and mass wasting for cohesive river banks. *J. Geophys. Res.* **2007**, *112*. [CrossRef]

Disclaimer/Publisher's Note: The statements, opinions and data contained in all publications are solely those of the individual author(s) and contributor(s) and not of MDPI and/or the editor(s). MDPI and/or the editor(s) disclaim responsibility for any injury to people or property resulting from any ideas, methods, instructions or products referred to in the content.